Master's thesis

Computational Physics

A Computational Study of the Surface Orientation Dependence of Tungsten Sputtering

Oliver Flinck

November 3, 2022

Supervisor: Dr. Fredric Granberg

Examiners: Prof. Kai Nordlund

Dr. Fredric Granberg

Tiivistelmä — Referat — Abstract

In this thesis, sputtering of several low- and high-index tungsten surface crystal directions are investigated. The molecular dynamics study is conducted using the primary knock-on atom method, which allows for an equal energy deposition for all surface orientations. The energy is introduced into the system on two different depths, on the surface and on a depth of $1\,\mathrm{nm}$. Additionally to the sputtering yield of each surface orientation, the underlying sputtering process is investigated. Amorphous target materials are often used to compare sputtering yields of polycrystalline materials with simulations. Therefore, an amorphous surface is also investigated to compare it's sputtering yield and process with crystalline surface orientations.

When the primary knock-on atom was placed on the surface all surface orientations had a cosine shaped angular distribution with little variation in the sputtering yield for most of the surface orientations. Linear collision sequences were observed to have a large impact on the sputtering yield when the energy was introduced deeper inside the material. In these linear collision sequences the recoils are traveling along the most close packed atom rows in the material. The distance from the origin of the collision cascade to the surface in the direction of the most close packed row is therefore crucial for the sputtering yield of the surface. Surface directions with high angles between this direction and the surface normal hence show a reduction in the sputtering yield.

The amorphous material had a little lower sputtering yield than the crystalline materials when the primary knock-on atoms was placed on the surface whereas the difference rose into several orders of magnitude when the energy was given at $1\,\mathrm{nm}$. It is impossible for linear collision sequences to propagate long distances in the amorphous material and therefore the angular distribution in both cases is cosine shaped. The amorphous material has no long range order and was therefore unable to reproduce the linear collision sequences, which are characteristic for the crystalline materials. The difference in the sputtering yield was hence up to several orders of magnitude as a result when the energy was introduced at $1\,\mathrm{nm}$ depth.

Contents

1. Introduction

Climate change is one of the biggest challenges of the century. Many countries are striving towards net-zero carbon emissions and new energy production forms are required to meet the global energy demand while still avoiding global warming. Investments are heavily made in renewable energy sources such as solar, water and wind to replace fossil fuels, but nuclear power is an often overlooked carbon-free energy source. Nuclear fission power plants have provided a stable flow of energy since the '50s, but have gained a bad reputation from the Chernobyl and Fukushima disasters. Another form of nuclear power, nuclear fusion, is a cleaner and safer form of nuclear energy, which uses two hydrogen isotopes as fuel instead of uranium or plutonium. Fusion could provide large amounts of carbon-free energy in the future together with the renewable energy sources. A proof of concept device is the confined magnetic fusion reactor ITER [1] under construction in southern France.

ITER is a tokamak fusion reactor, which is a torus shaped vacuum vessel containing magnetically controlled plasma. The most promising form of energy production with a tokamak is the fusing together of two isotopes of hydrogen, deuterium (D, $^2_1$H) and tritium (T, $^3_1$H). Deuterium can be extracted from seawater [2] but the supply of tritium is limited, expensive to manufacture and has a short half-life of 12.3 years. Therefore, future tokamak fusion reactors are planned to produce their own tritium inside the reactor via tritium breeding [2–4]. In tritium breeding enriched lithium, $^6_3$Li, is turned into tritium and helium by energetic neutrons in an exothermic reaction [5]. The D-T fusion reaction is the easiest to achieve with the highest collision cross-section at the lowest temperature (10^8 K) [6]. The reaction, $^2_1$H + $^3_1$H $\rightarrow$ $^4_2$He + $^1_0$n + 17.6 MeV, produces large amounts of energy, which is mostly released as the kinetic energy of the neutron. The plasma in the tokamak is controlled by strong magnetic fields but neutrons are, however, not affected by the confinement and will bombard the surrounding walls. The kinetic energy of the neutrons is transformed into heat in the innermost walls as they are slowed down. This heat is continuously extracted by a highly pressured water coolant and turned into electricity in the power plant.

The innermost components of the reactor are the blanket [3] and the diver-

tor [7]. The plasma facing wall materials have to withstand enormous heat as well as intensive particle irradiation from the plasma. Resistance to swelling, crack formation, surface reactions and specific defect processes such as subsurface helium bubbles is additionally required [8]. It is expensive to change the components inside the reactor and therefore a sufficient lifetime for the plasma facing walls is needed. For safety reasons an acceptable neutron resistance is connected with low long term activation and negligible or small retention of tritium is important [9]. Tritium is radioactive and a safety concern if it accumulates inside the plasma facing walls. The thermal conductivity has also to be high as the plasma facing walls are transporting the heat into the coolant.

The blanket protects the rest of the reactor components, such as structural materials and magnets, from the heat and particle irradiation. For ITER, beryllium has been chosen as the plasma facing wall material of the blanket modules as it has low plasma contamination and low fuel retention [3]. Beryllium can also be used as a neutron multiplier as neutrons are lost in the planed tritium breeding [5]. The divertor is located at the bottom of the vessel and it is positioned at the intersection of magnetic field lines. Here the flux of the bombarding particles is even greater and the divertor has to withstand heat fluxes up to $20\,\mathrm{MW/m^2}$ [7, 8]. Additionally to withstanding the neutron bombardment, the divertor is responsible for extracting impurities and other wastes, such as helium, from the plasma. With the highest melting point at $3680\,\mathrm{K}$ and lowest vapour pressure of all elements, tungsten has been chosen as the divertor plasma facing material for ITER [7,9]. Other advantages of tungsten is low sputtering, low tritium retention and high thermal conductivity [9–12]. The plasma is, however, sensitive to high-Z impurities and cools down at already low concentrations of tungsten atoms [9, 13–15]. Tungsten is also brittle at lower temperatures with a ductile to brittle transition temperature between $150\,^\circ\mathrm{C}$ and $400\,^\circ\mathrm{C}$ [9].

Sputtering from many different target material - ion projectile combinations has been studied both experimentally and computationally [16]. Tungsten has generally a low sputtering yield and shows little sputtering from the light H, D, T and He ions. However, helium can affect the surface and change it into W-fuzz or produce sub-surface helium bubbles [12, 17–22]. The main source of tungsten sputtering is from plasma impurities inside the reactor, which have much higher masses and can reach higher charge states than hydrogen and helium [9]. Most experiments are performed on polycrystalline surfaces and computer simulations focus mainly on sputtering from low-index surface orientations. Although low-index surface orientations show reduced sputtering compared to polycrystalline surfaces [23], polycrystalline tungsten will be used in ITER as it is much cheaper to manufacture.

A polycrystalline surface consists of many different crystal oriented grains and therefore it is not sufficient to only focus on low-index surface orientations. Furthermore, sputtering yields between low- and high-index tungsten surfaces are shown to vary significantly [23]. A study consisting of many different surface orientations is hence needed to get a greater understanding of the sputtering processes. Experimental sputtering yields are often compared with results from Monte Carlo based binary collision approximation simulations. These simulations utilize an amorphous target material and is a less tedious method than having to calculate an average sputtering yield from many different surface orientations. This assumes that sputtering from a large group of crystal directions or that the average over all surface orientations correspond to the sputtering yield of an amorphous material [23]. Some molecular dynamics studies have, however, investigated tungsten sputtering from several random surface orientations [24, 25], which is a more accurate representation of a polycrystalline surface.

In this thesis, tungsten sputtering is investigated for several low- and high-index surfaces. The molecular dynamics simulations are performed using the primary knock-on atom method with three different recoil energies. In the primary knock-on atom method kinetic energy is given to an already existing atom in the system, simulating energy transfer from an ion impact. The sputtering process for all surface orientations is hence compared with each other with an equal recoil energy at two different depths. Because experimental sputtering yields are often compared to simulations with amorphous target materials, an amorphous tungsten surface is also investigated. The sputtering yield and underlying process is then compared with the different oriented crystalline materials.

2. Radiation damage

2.1 Ion irradiation in bulk

All metals have their atoms organized in a crystal structure when the material is in a solid state. The three major crystal structures are Body Centered Cubic (BCC), Face Centered Cubic (FCC) and Hexagonal Close Packed (HCP), see Fig. 2.1. The close packed FCC and HCP structures have their atoms arranged as efficiently as possible whereas BCC is a more loosely packed structure. The atomic packing factor, the volume of the unit cell occupied by atoms, is 68% for BCC and 74% for FCC and HCP. Irradiation damage occurs in bulk materials when an energetic particle interacts with the atoms inside the material and distorts them from their lattice positions, which alters the crystal structure and damages the material.

(a) BCC   **(b)** FCC   **(c)** HCP
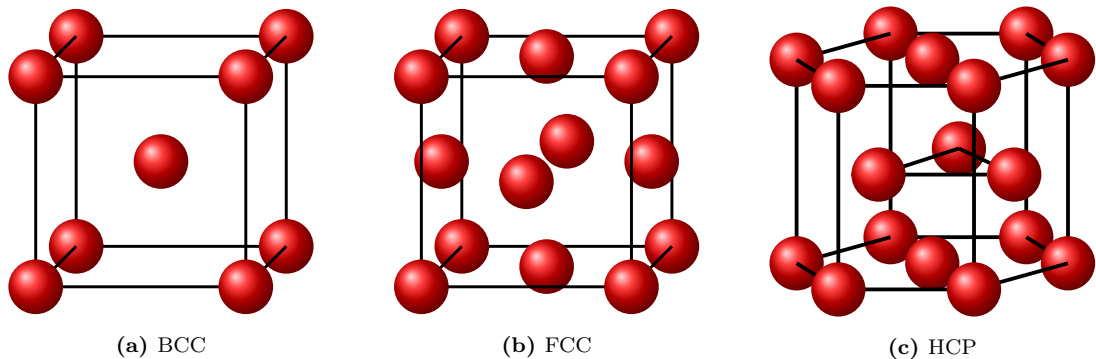
Figure 2.1: The three major crystal structures

Ions interact with atoms in the material via elastic or inelastic collisions depending on their mass and energy [26]. Binary elastic collisions are governed by a Coulomb potential between the ion's and atom's nucleus. The ion collides with the lattice atom and changes direction while loosing some energy to the nucleus in the collision. If the energy is greater than the threshold displacement energy the primary knock-on atom is recoiled from it's lattice position. The recoiled atom can contribute to the radiation damage by colliding with one or several other atoms and recoil them from their lattice positions, hence starting a collision cascade. For

inelastic collisions the electrons of the ion are interacting with the electrons in the lattice structure. The ion looses energy to the electrons as it travels through the material, which is effectively acting as a friction force on the ion. The path of the ion is, however, not distorted in this regime as the ion is much more massive than the electrons. These two types of interactions are called nuclear stopping power and electronic stopping power, respectively. The nuclear stopping is dominating at lower energies (keV) and for more massive ions whereas the electronic stopping is dominating at higher energies (MeV) and less massive ions [26].

Swift heavy ions are heavy high energetic ion projectiles, typically in the energy range $\geq$ MeV, where electronic stopping is dominating over nuclear stopping. Because their interactions with the atomic nuclei is negligible their paths are in the material undistorted and the ions move almost in a straight line. Large amounts of energy is disposed to the electrons in the ion's path, exciting them, while it is slowing down. In some materials these straight paths can be observed as ion tracks as excited electrons in the material leave ionized atom paths behind them. The electron system is equilibrated by transferring the excess energy by electron-phonon coupling [26, 27]. In materials with lower heat conductivity, i.e. insulators, the excess energy has nowhere to go and a few nanometer wide cylindrical thermal spike is created around the ion track, which can evaporate surface atoms in a jet. In metals where the heat conductivity is high, the ion track has less time to form before the excess energy has been dispersed and might not be observed at all. It has been suggested that swift heavy ions can help to recover damaged materials. The heat from ion tracks could remove defects and recrystallize the material [26].

The atomic structure inside a material can be altered and damaged in different ways when ions recoil atoms from their lattice positions. Point defects, such as interstitials and vacancies illustrated in Fig. 2.2, are crystallographic defect structures consisting of only one or a couple of atoms. Interstitials are atoms which occupy positions in the lattice where there normally would not be any atoms. This puts additional stress on the material and distorts the surrounding lattice, which can expand the material and cause it to swell. If an interstitial atom is of the same type as the surrounding material, it is a self-interstitial defect and otherwise an impurity interstitial. Interstitial defects do not have to be atoms recoiled from their lattice positions and can consist of embedded ions trapped in the material. Embedding ions in a material is a useful tool in the semiconductor industry where semiconductors are doped with impurities to change the number of charge carriers and hence the electrical conductivity of the material. Impurity interstitials can also consist of small atoms, e.g. hydrogen, which have diffused into the material. When an atom is knocked from the lattice position, the position can remain unoccupied and an

empty space is created in the lattice. These unoccupied lattice positions are known as vacancies. Neighboring lattice atoms can jump into them and hence move the vacancy around in the material. If the removed atom remains close to the vacancy as an interstitial, the defect is known as a Frenkel pair.

Point defects can cluster together and collapse into larger more energetically favorable defect structures, such as dislocation loops and stacking-fault terahedra [28]. Other common structural defects are for instance edge dislocations, screw dislocations and a mixture of them both. Dislocation loops can create or remove an extra plane of atoms within the material. Stacking-fault tetrahedra are pyramidal defect structures in FCC materials, which are built from stacking faults on intersecting $\{1\,1\,1\}$ planes [28]. These are extremely stable and nearly immobile [29].

2.2   Sputtering

Sputtering was discovered in the mid 19th century. It took, however, half a century before it was proven that the metallic deposition on the glass walls of discharge tubes was the result of sputtered ionized atoms [30]. Physical sputtering is a near surface event where the projectile undergoes energetic binary collisions with lattice atoms in the top surface layers [27]. After up to several recoils in the material, a surface atom is ejected when given enough kinetic energy to overcome the surface binding energy. How sensitive a material is to sputtering is measured by it's sputtering yield (Y), which is calculated according to Eq. (2.1).

$$Y = \frac{\text{number of ejected particles}}{\text{number of incoming projectiles}} \tag{2.1}$$

In addition to physical sputtering, sputtering can occur as a result of chemical surface reactions, chemical sputtering. In chemical sputtering the sputtering yield of a material can be modified by reactive ions [27]. Unstable molecules and compounds can be created at the surface to increase the sputtering and by choosing ions which form strong compounds on the surface, such as carbides or oxides, it can be reduced. Chemical surface reactions with atoms in the atmosphere can also cause surface erosion. For insulators sputtering is possible as a result of the ion leaving a localized excitation, which upon decay can create a primary knock-on atom [27]. Instead of an ion projectile, molecules and ion clusters can serve as the bombardment projectile. The cluster can be deposited at the surface, cluster deposition, or if more energetic, damage several atom layers and create a crater on the surface [31]. Physical sputtering from metals by ion bombardment is, however, the most common studied topic [30].

Depending on the bombardment energy, the sputtering process is categorized into the single knock-on regime, the linear cascade regime and the spike regime [27, 30, 32]. These are illustrated in Fig. 2.2. In the single knock-on regime, the incoming particles have either low mass (e.g. H, D and He) or low energy. The ion can directly hit a surface atom and eject it, or undergo a few collisions in the near surface layers before it is backscattered towards the surface. The energy is not, however, large enough to recoil more than a few atoms from their lattice positions. In the linear cascade and spike regimes, on the other hand, the incidence energy is high enough to start collision cascades in the material. The primary knock-on atom is recoiled from it's position with enough energy to recoil several other atoms in it's path. Several binary collisions hence lead to recoils of higher generations, a collision cascade. The density of recoiled atoms in the linear cascade regime is

too low for collisions between moving atoms to be likely. In the spike regime, the density of recoiled atoms is much higher and almost all atoms inside a small volume are in motion. Therefore, collisions are mainly happening between moving atoms leading to non-linear effects. The kinetic energy of the atoms can, depending on the material, lead to very high temperatures within the spike volume and amorphize the material [33].
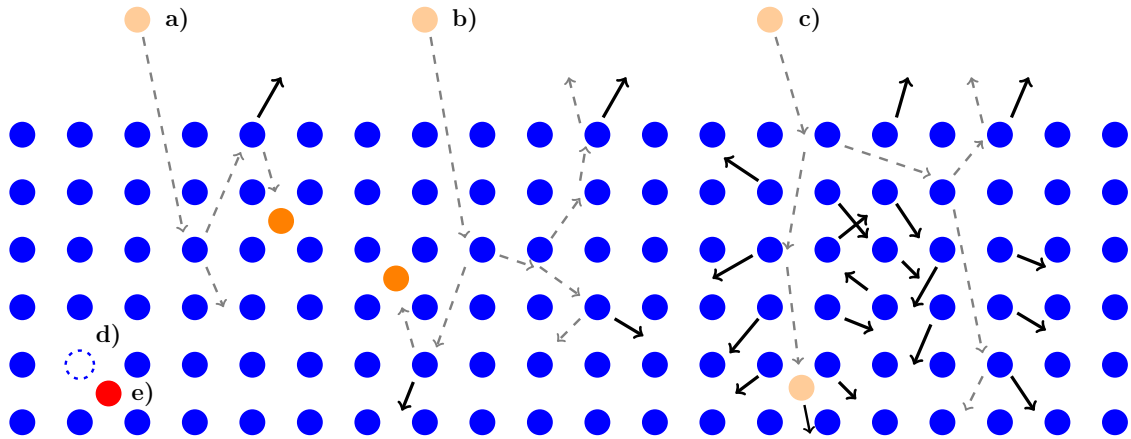

Figure 2.2: The three regimes of sputtering: a) single knock-on, b) linear cascade and c) spike regime. Additionally a d) vacancy and e) interstitial are illustrated.

Other factors affecting the sputtering yield are the mass difference between the projectile and target material, the angle of incidence, the materials crystallinity, surface crystal orientation, texture of the surface, the surface binding energy, *etc.* [11, 23, 25, 32, 34–36]. The surface binding energy, which is often assumed to be the same as the heat of sublimation, depends on the atomic density of the surface [11]. Structural defects such as edge atoms, adatoms and atoms from steps on the surface have lower surface binding energies and are easier to remove from the surface [32]. The sputtering yield increases with more oblique bombarding angles and can be significantly higher than for normal incidence bombardment [34]. The maximum in the sputtering yield is shortly followed by a sudden drop, as projectiles start to reflect from the surface instead of penetrating it when the bombardment angle is too steep [25, 37]. The fraction of projectiles which are reflected from the surface is measured by the reflection yield. Crystalline materials have orientations where the lattice structure opens up between planes and rows making free transparent paths in the material. These are channeling directions, which in BCC materials are for instance $\langle 1\,0\,0 \rangle$ and $\langle 1\,1\,1 \rangle$ [38]. If incoming projectiles are directed in an angle parallel to a channeling direction they can move trough the material nearly unstopped and travel long distances, which reduces the sputtering yield significantly as the energy from the projectile is dispersed deep within the material [39]. The

channeling effect for different surface orientations is presented as the penetration depth of ions in channeling maps [23, 25, 38].

In experiments, the sputtering yield can be measured with the weight-loss method. In the weight-loss method the mass of the target is measured before and after the experiment and the change in mass determines the sputtering yield. A drawback for this method is that the sputtering yield only depends on the change of mass. Some ions from the irradiation may have been embedded in the target material, which increases the mass of the sample. In a similar way the sputtering yield can be determined by measuring the material's thickness before and after the experiment. A few other measurement techniques are Rutherford backscattering, spectroscopy and field ion microscopy [27, 34]. For the sputtered atoms the energy- and angular distributions are often measured as $Y(E)$ or $Y(\theta)$, respectively. These distributions are helpful to get a broader understanding of the underlying sputtering mechanisms. For instance, forward sputtering has been observed to be favourable during ion bombardments at oblique angles [34]. Wehner spots, which will be discussed in the next chapter, is a phenomena contributed to sputtering in specific outgoing angles for single crystalline materials.

Instead of being something harmful, sputtering can be used as a tool in various industrial applications [34, 40–44]. Sputtered atoms can be redeposited on surfaces creating thin coats or as a precise tool for growing thin films. Other applications which utilize sputtering are for instance ion milling, dry etching and secondary ion mass spectroscopy.

3. Motivation

3.1 Background

Wehner was studying sputtering from different metals and surface orientations in the '50s when he came across anisotropic emission patterns, now known as Wehner spots [45, 46]. Sputtered atoms formed different emission patterns on the collectors depending on the crystal directions of the samples. The pattern is formed in the sputtering direction of the most close packed crystal directions and hence reflects the characteristic crystal structure on the surface of the material. His conclusion was that a sequence of atomic collision processes inside the material was responsible for the emission pattern [47].

Focusons, as the linear collision sequence is called, are likely one reason for the emission patterns. Focusons are a specific type of a linear collision cascade that can only propagate in the most close packed direction in the crystal lattice, which is the $\langle 1\,1\,1 \rangle$ direction in BCC and $\langle 1\,1\,0 \rangle$ direction in FCC. In the focusing effect, the atoms have to collide with each other in a sequence so that the collision angle between them and the most close packed atom row is approaching zero as the cascade is moving through the material [48]. The propagation hence becomes more focused in the most close packed row and the energy is therefore more effectively transferred in the most closed packed direction from one atom to the next in the collision sequence [48, 49]. As a result the collision sequence can propagate further in the material than other linear collision cascades.

There can also occur so called assisted focusons, which do not move in the most close packed directions but in other highly symmetrical directions. These emission patterns are from the next-nearest neighbor atom rows surrounding the focuson directions and are more diffuse emission patterns than patterns from the most close packed rows. The $\langle 1\,0\,0 \rangle$ direction is a next-nearest neighbor crystal direction for both BCC and FCC materials [32]. Metals with the BCC structure have a lower packing factor than FCC metals. Therefore, BCC metals sputter in the $\langle 1\,0\,0 \rangle$ direction at already lower irradiation energies than FCC metals [49].

3.2   Previous sputtering investigations

Sputtering has been the topic of many experimental and computational studies over the last decades. Therefore, the sputtering yield is already known for many different combinations of target materials and projectiles [16]. Tungsten has been chosen as the divertor armour material in the ITER fusion reactor for it's low sputtering yield. It is important to keep impurities away from the plasma as it cools the plasma down and hinders fusion reactions, which is more pronounced with high-Z elements. Furthermore, massive particles inflict higher damage to the surrounding walls and are therefore the main source of tungsten sputtering in the reactor [9]. It is favorable to keep the sputtering yield under 1, below unity, for plasma facing materials to avoid runaway erosion [50–55]. Tungsten is one of the heaviest materials inside the reactor and it is therefore important to keep its erosion below unity at fusion relevant conditions.

Tungsten self-sputtering was experimentally studied for perpendicular irradiation in the energy range 100 eV-10 keV [14]. Unity is avoided as long as the bombardment energy stays below 1 keV, which is in good agreement with the results from Ref. [50, 56]. It rises, however, to $Y = 2.30$ and $Y = 3.82$ for irradiation energies of 3 keV and 10 keV, respectively. Additionally to compare the experimental sputtering yields to TRIM.SP [57] calculations, the effect of the angle of incidence was computationally studied for a few bombardment energies. The calculations showed maximum sputtering for the angle of ion incidence at around 60° where unity was already reached at 400 eV. At 2500 eV the sputtering yield was around 4.5, which surpasses the sputtering yield from perpendicular 10 keV bombardment. For several angles of incidence tungsten self-sputtering was experimentally studied at 350 eV and 2 keV [51]. The gross yields (self-sputtering yield + reflection yield) for both energies were 0.30 and 1.76 for perpendicular bombardment while 1.16 and 4.44 with the angle of incidence 60° off-normal. In a study by Bay *et al.* [58] a tungsten surface was bombarded by 4 keV H ions at the angles of 0°, 60° and 80° off surface normal. The corresponding sputtering yields were $2.1 \cdot 10^{-3}$, $9.6 \cdot 10^{-3}$ and $32.8 \cdot 10^{-3}$, which shows a significant increase in sputtering for more oblique angles.

Experimentally sputtering from polycrystalline surfaces is mostly studied although crystal orientation dependent sputtering has been known for several decades [11]. The effect of crystal oriented erosion can, however, be experimentally studied with polycrystalline surfaces by bombarding an area with multiple grains. In an experiment by Ran *et al.* [11] the surface evolution of the grains was followed by taking real time *in situ* observations with a scanning electron beam during 30 keV Ga bombardment. The surface erosion from different grains and therefore different

crystal orientations was vastly different. Grains with low-index surface orientations showed much less sputtering due to the strong channeling effect and higher surface binding energy than grains with high-index surfaces. Similar results was found both experimentally and computationally with 30 keV Ga ions in Ref. [23]. Surfaces in the $\langle 1\,1\,1 \rangle$ and $\langle 0\,0\,1 \rangle$ directions showed overall least sputtering due to strong channeling, with sputtering yields around 2. Most sputtering was obtained around the $(2\,1\,3)$, $(3\,1\,5)$ and $(3\,1\,9)$ surface orientations with sputtering yields around 8.

Channeling can only occur in crystalline materials and was studied for single crystalline tungsten [39]. In the experiment, a $(1\,0\,0)$ surface was irradiated with a 30 keV Ga focused ion beam. The sample was rotated vertically from 0° to 55° while the sputtering yield is continuously measured throughout the rotation. Additionally to the initial $\langle 1\,0\,0 \rangle$ direction, the low-index $\langle 2\,1\,0 \rangle$ and $\langle 1\,1\,0 \rangle$ crystal directions are in this region. Initially the sputtering yield is low as the $\langle 1\,0\,0 \rangle$ direction is a loosely packed channeling direction. As the sample becomes more tilted, the channel closes and already at a 7° rotation the sputtering yield has increased. The sputtering yield increases steadily with the angle of incidence until a 26° tilt, where the $\langle 2\,1\,0 \rangle$ direction is located and a narrow channel opens up. The sputtering yield rises again until it is reduced by the $\langle 1\,1\,0 \rangle$ channeling direction at 45°. The maximum sputtering yield is reached at 54° where it is 9-10 times higher compared to the perpendicular bombardment in the beginning. Although the sputtering yield rises with the angle of incidence it is clearly reduced for bombardment angles in parallel with channeling directions. Iron, which is also a BCC material, produced similar results as tungsten in the study and was additionally tilted into the $\langle 3\,1\,1 \rangle$ and $\langle 1\,1\,1 \rangle$ direction. These are channeling directions as well and especially the $\langle 1\,1\,1 \rangle$ direction showed a significant reduction in the sputtering yield.

Several computational studies with many different bombardment ions, angles and energies have been performed on low-index tungsten surfaces [19, 20, 25, 50, 52, 54, 59]. During perpendicular He irradiation the $(1\,1\,0)$ surface has the highest sputtering yield of the often investigated $(0\,0\,1)$, $(1\,1\,0)$ and $(1\,1\,1)$ low-index surfaces. This is in good agreement with the channeling map in Ref. [25], as the $(0\,1\,1)$ plane has the highest atom density of all three crystal orientations. Therefore, a collision between the ion and a surface atom is more probable compared to surfaces with lower densities. For a $(0\,0\,1)$ surface unity was reached by self-sputtering at around 1 keV [52], which is in good agreement with the experimental results.

The effect of tungsten fuzz have also been studied as helium is produced in the D+T fusion nuclear reaction [12, 17–22]. W-fuzz is created when tungsten is exposed to high flux low energy helium bombardment at temperatures of $900\,\mathrm{K} - 2000\,\mathrm{K}$ [22]. The growth is proportional to the square root of the exposed irradiation time and

creates nano-sized foam at the surface [17,60]. This effect can naturally occur in fusion reactors when extremely hot helium plasma interacts with the plasma facing wall materials. A sample of W-fuzz was grown to a thickness of $\backsim 1\,\mu\text{m}$ before it was irradiated with $85\,\text{eV} - 235\,\text{eV}$ Ar ions [17]. The sputtering yield is consistently lower for the fuzzy surface compared to a smooth one, up to a factor of 10. The line-of-sight deposition is a possible explanation to the lower sputtering yield for W-fuzz. Atoms sputtered in a broader distribution at low energies and closer to the surface normal when the bombardment energy was increased, with no significant difference between the smooth and fuzz surface. Therefore, in the lower energy cases, the ejected atoms fail to escape the nanostructure and are redeposited in the fuzz, whereas for higher energies the ejected atoms are able to reach the surface as they sputter in a narrower angular distribution. The fuzz-thickness dependency was investigated at $110\,\text{eV}$ and the sputtering yield saturated at almost $\backsim 10\%$ compared to a smooth surface when the fuzz-thickness was greater than $1\,\mu\text{m}$. Pure tungsten $(0\,0\,1)$, $(1\,1\,0)$ and $(1\,1\,1)$ surfaces have also been compared to surfaces containing sub-surface helium bubbles [19,20]. The effect on the sputtering yields was, however, negligible.

Additionally to tungsten fuzz, the sputtering yield is affected by the surface roughness of crystalline tungsten. Tungsten pellets were constructed from different particle sizes, $<\,1$, 12, 44-74 and 149-297 µm, to achieve differences in surface roughness. The corresponding sputtering yields after $2\,\text{keV}$ Ar bombardment were 6.82, 2.26, 1.31 and 0.97 [13], which shows a 7 times reduction in sputtering for the roughest sample. Single crystalline $\langle 1\,1\,1\rangle$ tungsten whiskers were utilized to reduce the sputtering yield by a factor of 3 compared to smooth single crystalline tungsten [61], for $4\,\text{keV}$ He ion bombardment. In both cases the ejected atoms are trapped in the surface microtopography and the $\langle 1\,1\,1\rangle$ oriented whiskers further reduced the sputtering yield by absorbing ions due to channeling. Computationally the effect of surface roughness has shown an increase in sputtering for small amount of surface roughness [53]. A maximum is seen for surfaces with a peak to peak height difference of approximately $25\,\text{Å}$ and a surface height standard deviation of approximately $6\,\text{Å}$. For rougher surfaces is a reduction in the sputtering yield observed. Surface roughness and configuration does not, however, affect the sputtering direction [49].

3.3   Simulations

Computer simulations has been a powerful tool in materials research for several decades. The simulations give an insight on events at an atomic scale and an opportunity to analyze the results in a different way compared to experiments. Two different commonly used computer simulation methods are binary collision approximation (BCA) and molecular dynamics (MD).

In BCA a projectile travels through the material and interacts with elastic binary collisions between itself and a target atom. The scattering angle and energy loss is calculated by solving the classical scattering integral between two colliding particles by numerical integration. If the energy transferred from the projectile to a targeted atom is greater than the threshold displacement energy the atom is recoiled and starts a cascade on it's own. The projectile moves in a straight line between each collision and during this time energy is only lost through electronic stopping. In typical BCA codes, the distance to the next atom is randomized and calculated from a probability distribution, which only depends on the atomic density of the target material. The target material has hence no crystal structure and is amorphous. There are, however, a few BCA codes where the crystallinity of the target material is implemented. In contrast the evolution of an atomic or molecular system is calculated dynamically for a given period of time in MD simulations. In MD the positions and velocities of the atoms are defined at the beginning of the simulation, and hence the material has always a known structure. The movement of atoms are calculated by solving the Newtonian equations of motion for each atom in the many-body system.

A widely used BCA program is the Monte Carlo (MC) based SRIM [62] code. SRIM is used for instance to calculate the penetration depth of ions in materials, damage cascade profiles and in sputtering simulations [63]. The BCA simulation method has, however, some known weaknesses in the field of sputtering. At low energy irradiation where many-body collisions dominate and play a significant role, the approximation of binary collisions fails [24, 32]. An other drawback is that BCA codes generally consider the target material as amorphous and hence do not take the material's structure and crystalline effects into account. The amorphous structure has not, however, a huge impact for high energy irradiation. The heat spike effect can create a liquid-like zone in the energetic ion's path and an initial amorphous structure is therefore a good approximation. The sputtering yield of polycrystalline materials are often compared with SRIM calculations under the assumption that they should give the same result. The reasoning is that the sputtering yield over all crystal directions averages to the amorphous sputtering yield or that groups of random

crystal orientations has the same sputtering yield as the amorphous material [23].

For BCA codes, the surface binding energy is a sensitive parameter for the accuracy of the simulation. The often used value is the heat of sublimation for the target material. For a $(0\,0\,1)$ tungsten surface the surface binding energy was calculated by LAMMPS [64] using three different many-body potentials to $11.75\,\text{eV}$, which is around 35% higher than the heat of sublimation [59]. It has also been shown that the energy required to remove an atom from a relaxed crystalline surface is typically 40% greater than the heat of sublimation [32]. By using the calculated surface binding energy the sputtering yield from both BCA and MD was in good agreement with each other. However, by using the heat of sublimation as the surface binding energy parameter the sputtering yield was overestimated by almost a factor of 2 at $500\,\text{eV}$ Be irradiation. Although LAMMPS and the BCA code ITMC [65] produced similar total sputtering yields, the angular distribution was very different. Due to the amorphous material in the BCA simulations, the distribution was uniform and failed to reproduce Wehner spots in the $[1\,1\,1]$ directions, which were present in all three MD simulations.

By randomly rotating a simulation cell and taking the averaged sputtering yield from all surface orientations, a more accurate representation of a polycrystalline surface is simulated in MD. Experimental values were compared to both SRIM calculations and the results from the MD code PARCAS [66] in a study by Marenkov *et al.* [24]. The sample was irradiated with low energy Ar ions, $85-200\,\text{eV}$, and both the sputtering yield and angular distribution was studied. The experimental and MD angular distributions are in good agreement with each other in the range $100-200\,\text{eV}$. Although the distribution from SRIM calculations had a similar shape it was shifted towards lower angles. At the lowest energy, $85\,\text{eV}$, the SRIM distribution is completely different from the other two with its peak around 35° compared to the experimental with its peak around 80°. The MD distribution shows a similar trend as the experimental, although they do not match each other as well as for the higher energy cases.

In a similar way, tungsten sputtering from random oriented surfaces as well as the $(0\,0\,1)$, $(0\,1\,1)$ and $(1\,1\,1)$ low-index surfaces was investigated [25]. The surfaces were bombarded with He and Ar ions with energies up to $1000\,\text{eV}$ and with incidence angles between $0°-87°$. Large variations in the sputtering yields between the random oriented surfaces occurred and their average sputtering yield was compared to the low-index surfaces. The magnitude of the sputtering yields were different between all low-index surface orientations for all bombardment angles. Although the sputtering yield was similar between the low-index and averaged random surface orientation, it was clear that the averaged sputtering yield did not correspond to any of the

low-index surfaces. The random sputtering yield was higher at large bombardment angles, but it could be explained by the surface morphology, which is much rougher for the random surface orientations. The low-index surfaces also had channeling in some directions, which reduced their sputtering yields. In the angular distributions, peaks were observed in some outgoing angles for the low-index and random surfaces, whereas the averaged distribution of all random surfaces was much broader without any individual peaks.

In the study by Schlueter *et al.* [23] experimental data is compared to simulations performed by both PARCAS and the BCA code IMSIL [68]. The experiments and simulations on tungsten are performed with 30 keV Ga ions on several different low- and high-index surface orientations. The sputtering yields are in excellent agreement between all different methods and crystal directions. Additionally to the sputtering yields, the energy to recoils in the top 2 nm was measured independently by MDRANGE. The low-index channeling directions have a low recoil energy in the near surface layer whereas the disposed energy is orders of magnitude larger for the high-index surfaces, which corresponds to much higher sputtering yields. The linear correlation between the two is shown in Fig. 3.1. The amorphous surface does not, however, follow the linear trend of the crystalline surfaces and the sputtering yield is lower than predicted. The sputtering yield changed also constantly with differ-
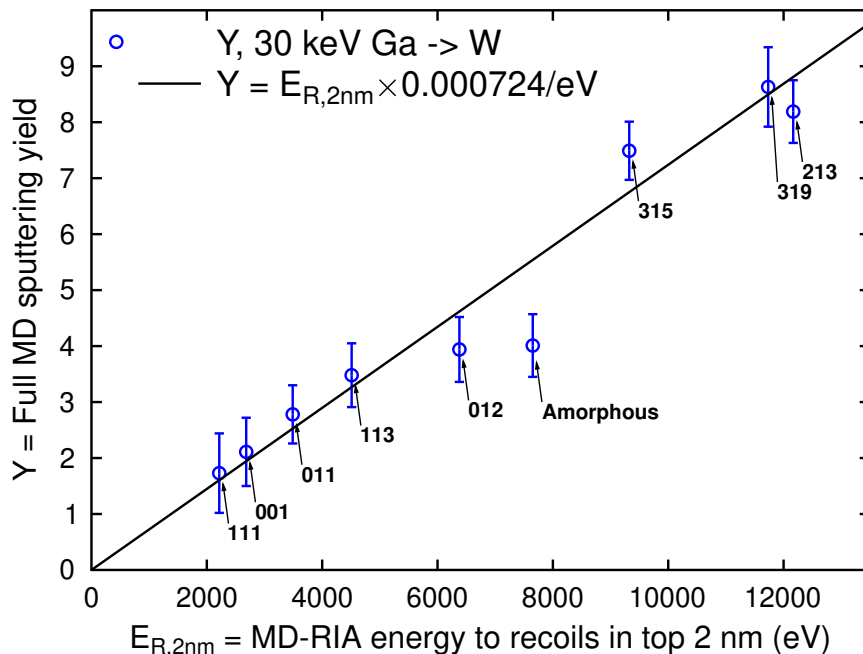

Figure 3.1: The correlation between the sputtering yield and the amount of energy deposited to recoils in the top 2 nm for several tungsten surface orientations and an amorphous tungsten surface. The graph is from Ref. [67] and modified by adding the amorphous surface from the same data set.

ent surface orientations and hence there were not any groups of crystal directions that would have corresponded to the amorphous sputtering yield. Simulations performed with BCA on both polycrystalline and amorphous tungsten had the average sputtering yields of 4.71 and 2.29, respectively, which is significantly different.

As simulating sputtering yields from many different single crystalline surface orientations is time consuming and tedious amorphous surfaces are often used as a substitute for polycrystalline materials. Crystalline materials have, however, many different surface effects which are not reproduced by amorphous materials. When SRIM is compared to polycrystalline experiments it has overestimated the sputtering threshold energy and the sputtering yield at low energy irradiation [24, 63, 69]. Several studies have also shown higher sputtering yields for amorphous materials compared to the $(0\,0\,1)$, $(0\,1\,1)$ and $(1\,1\,1)$ low-index surfaces [23, 36, 70]. The energy is deposited in the near surface layers in amorphous materials whereas the ion can penetrate deep into the material for the low-index surfaces due to channeling. Channeling has been studied for many surface orientations and are presented in channeling maps [23, 25, 38]. More energy is also dispersed in the top most surface layers for high-index surfaces compared to an amorphous material. Furthermore, experimental tungsten samples may have a preference towards low-index surfaces as a result of the processing methods [25]. For single crystalline materials atoms sputter in specific directions and create emission patterns, which the Monte Carlo based BCA simulations failed to reproduce [59]. It is further shown that the sputtering yields of amorphous and polycrystalline tungsten is vastly different [23]. For these reasons, experimental sputtering yields from polycrystalline materials should not be directly compared to Monte Carlo based BCA simulations.

4. Methods

4.1 Molecular dynamics

Molecular dynamics (MD) is a computational method for simulating atomic or molecular systems. The movement of the particles are dynamically followed during the simulation and several different physical quantities can be calculated as the system evolves in time. In the simulations the Newtonian equations of motion are numerically solved to calculate the trajectories for the particles for each time step. As the computational capacity of computers has increased during the last decades, MD has become a powerful tool in addition to both experimental and theoretical studies in fields like materials sciences, chemistry and biology. The basic steps and a few common features of an MD loop are illustrated in Fig. 4.1.

In the beginning of a simulation the initial positions and velocities are defined for each atom. The initial velocities are randomized according to the simulation temperature by the Maxwell-Boltzmann distribution. The system starts to evolve by calculating the force for each atom and Newton's equations of motion are numerically solved to get the acceleration. The relationship between the force, $\mathbf{F}_i$, and the interatomic potential, $V(\mathbf{r}_i)$, for each atom is

$$\mathbf{F}_i(\mathbf{r}_i) = m_i \frac{d^2\mathbf{r}_i}{dt^2} = m_i\mathbf{a}_i = -\nabla V(\mathbf{r}_i) \tag{4.1}$$

where $\mathbf{r}_i$ is the position, m_i the mass and $\mathbf{a}_i$ the acceleration. Simulated systems usually consists of several thousands or even up to hundreds of millions atoms. The interatomic potentials are range dependent and their contribution are generally negligible at longer distances. Therefore, a neighbor list is made for each atom, which is unchanged for several iterations and only contains atoms inside a defined cut-off radius. In the force calculations, only atoms in the neighbor list are evaluated for each atom, which reduces the computational cost of the simulation.

Set initial parameters, conditions,
positions $\mathbf{r}_i(t_0)$ and velocities $\mathbf{v}_i(t_0)$

Calculate forces $\mathbf{F}_i(\mathbf{r}_i)$ and $\mathbf{a}_i \;=\; \mathbf{F}_i/m_i$

Solve the equations of motion
Update positions $\mathbf{r}_i(t_n) \;\rightarrow\; \mathbf{r}_i(t_{n+1})$
and velocities $\mathbf{v}_i(t_n) \;\rightarrow\; \mathbf{v}_i(t_{n+1})$

Apply periodic boundary conditions, thermostats etc.

Calculate physical quantities
Energy, temperature, pressure etc.

Update time step
$t_{n+1} \;=\; t_n \;+\; \Delta t$

No

$t_{n+1} > t_{max}$
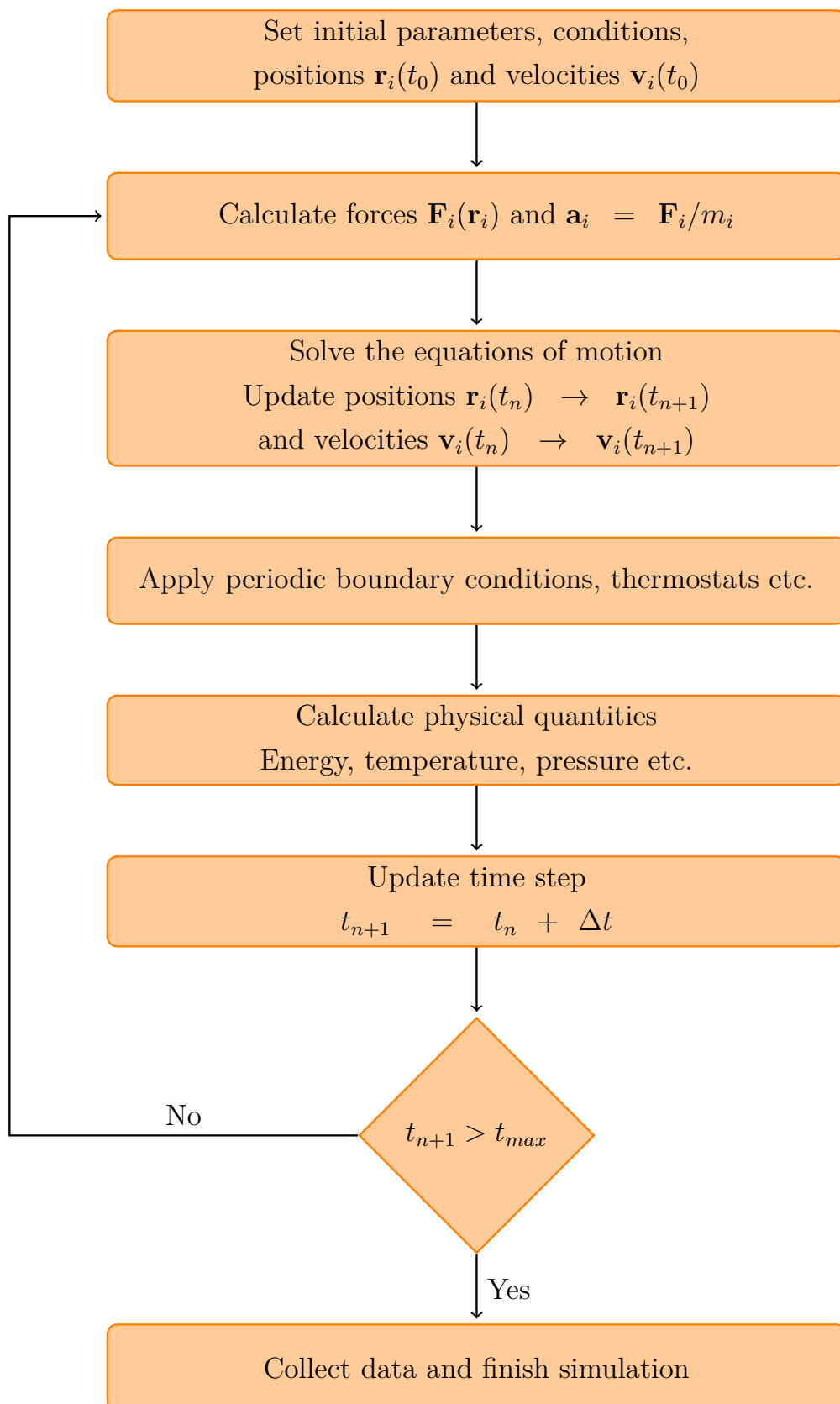
Yes

Collect data and finish simulation

Figure 4.1: The basic steps of an MD loop

In general an interatomic potential can be written as Eq. (4.2) where the total potential energy of the system V_{tot} is a sum of a series of terms over all N atoms. Here V_1 is the one-body term, V_2 is the two-body term and V_3 is the three-body term, *etc.* The potential energy depends on the atom positions, $\mathbf{r}$, and to make sure that no atom pairs are calculated multiple times, the rule $i < j$ and $j < k$ is followed. Because the V_1 term only effects the atom if it's inside an external field it is often left out for simplicity. Every atom type needs an own interatomic potential, e.g. three different potentials are needed if a system consists of two types of atoms.

$$V_{\text{tot}}(\mathbf{r}) = \sum_i^N V_1(\mathbf{r}_i) + \sum_{i,j}^N V_2(\mathbf{r}_i, \mathbf{r}_j) + \sum_{i,j,k}^N V_3(\mathbf{r}_i, \mathbf{r}_j, \mathbf{r}_k) + \cdots \tag{4.2}$$

Interatomic potentials are categorized in two major groups, pair potentials and many-body potentials. In a pair potential only the first two terms are used, where V_2 depends on the distance between atom i and j. An example of a pair potential is the Lennard-Jones potential [71, 72], which can be used in simple noble gas simulations with good accuracy. Another widely known pair potential is the Morse potential [73]. Pair potentials are, however, not very accurate for calculating physical properties of more complex systems and therefore many-body potentials are used in most simulations.

Many-body potentials are more complex and therefore more accurate but they also have an increased computational cost. The Stillinger-Weber potential [74], Tersoff potentials [75, 76] and Embedded-Atom Method (EAM) potentials [77] are many-body potentials. The Stillinger-Weber potential, where the three-body term depends on the bond angle between atoms, was originally developed for silicon but various versions of it has been made for many different materials. Metals are in general well described by EAM potentials

$$V_{\text{EAM}}^{\text{tot}} = \sum_i^N F_i \left(\sum_j \rho(\mathbf{r}_{ij}) \right) + \frac{1}{2} \sum_{ij}^N V_2(\mathbf{r}_{ij}) \tag{4.3}$$

where F_i is the embedding function, $\rho(\mathbf{r}_{ij})$ is the electron density and V_2 is the two-body term, which depends on the distance between two atoms. For covalently bonded materials bond order potentials (BOP) are used. Tersoff potentials are widely used BOP potentials and they have repulsive and attractive terms, which are exponential functions similar to the Morse potential, and the strength of the attractive term depends on the environment of the atom. Other BOP potentials are the Brenner potential [78] and the Finnis-Sinclair potentials [79]. Covalent bonds are also described by modified embedded atom method (MEAM) potentials [80], where angular dependency terms have been added in the embedding function.

After the force calculations, the positions and velocities of the atoms are updated. There are several different algorithms which can be used in the trajectory calculations. The standard Verlet algorithm [81] is based on the Taylor expansion of the atomic positions with respect to a small time perturbation $t \pm \Delta t$. The positions are updated using Eq. (4.4), where $\mathbf{r}$ is the position, $\mathbf{a}$ the acceleration and Δt the time step.

$$\mathbf{r}(t + \Delta t) = 2\mathbf{r} - \mathbf{r}(t - \Delta t) + \Delta t^2 \mathbf{a}(t) \tag{4.4}$$

The problem with the original Verlet algorithm is that the velocity is always one step behind, Eq. (4.5). The velocity is important for calculating the kinetic energy of the atoms at the given time t. Thermostats, which will be discussed later in this section, also use the atomic velocities to scale the temperature of the system.

$$\mathbf{v}(t) = \frac{\mathbf{r}(t + \Delta t) - \mathbf{r}(t - \Delta t)}{2\Delta t} \tag{4.5}$$

The leapfrog algorithm [82] and velocity Verlet algorithm [83] have been developed to solve the velocity calculation problems. The velocity Verlet algorithm updates the position, Eq. (4.6), and velocity, Eq. (4.7), at the same time step and is widely used in MD simulations.

$$\mathbf{r}(t + \Delta t) = \mathbf{r}(t) + \mathbf{v}(t)\Delta t + \frac{1}{2}\Delta t^2 \mathbf{a}(t) \tag{4.6}$$

$$\mathbf{v}(t + \Delta t) = \mathbf{v}(t) + \frac{\mathbf{a}(t) + \mathbf{a}(t + \Delta t)}{2}\Delta t \tag{4.7}$$

Predictor-corrector methods are a different way to calculate the trajectories of the atoms in the system. As the name suggests, the positions and velocities are first predicted before a correction is made to the initial predictions. We will not go deeper into this method in this thesis and only mention it as an alternative as the common Gear algorithm [84] is used in PARCAS.

The accuracy of a simulation largely depends on the length of the time step with a trade-off between accuracy and the computational cost. A shorter time step gives more accurate atomic trajectories but at a higher computational cost whereas simulations are faster with larger time steps. If an atom moves too much during one time step, it can lead to unphysical behaviours and the total energy conservation of the system might be violated. The time step should be shorter than any oscillation periods in the system to conserve the total energy. A good rule of thumb is to choose a time step of a few femtoseconds [85]. Another way to maintain the accuracy of the simulation is to utilize an adaptive time step, which changes during the simulation depending on the velocities and energies of the atoms in the system. It can be shorter if there are suddenly large amounts of energy introduced to the system, e.g.

ion bombardments, where the time step has to be short to ensure the accuracy. This also allows for faster simulations as the time step can be longer when the energies in the system are lower.
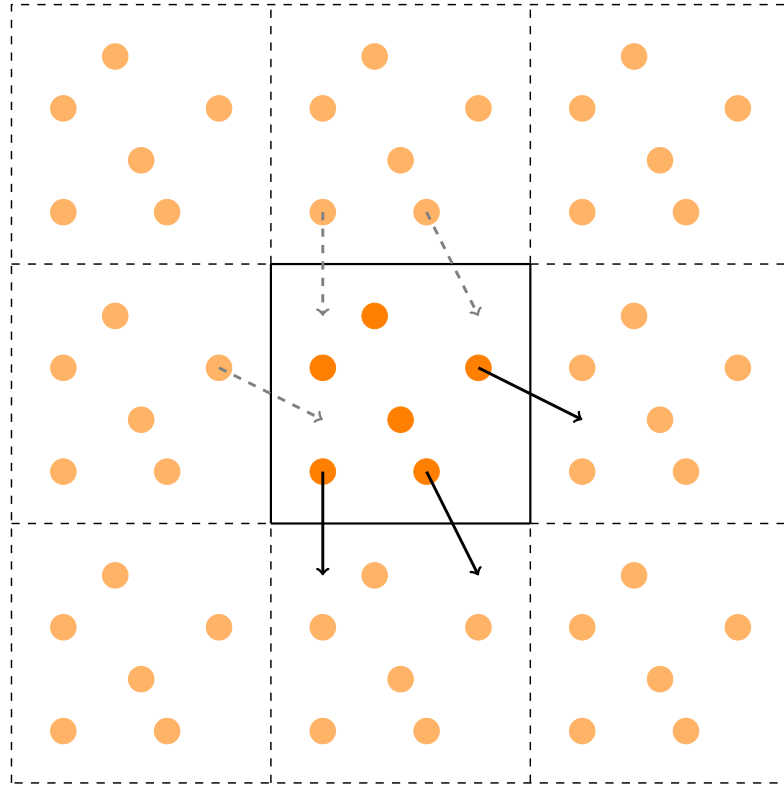

Figure 4.2: Periodic boundary conditions illustrated in 2D

After the basic steps of an MD loop, it is time to take a look at some common features used in MD simulations. The use of periodic boundary conditions (PBCs) is a way to effectively extend the cell in any combination of the x-, y- and z-directions. By applying PBCs virtual identical cells of atoms are placed around the original atomic cell, illustrated in Fig. 4.2. The atoms interact with atoms from the virtual cells and if an atom leaves the cell at one side will it reappear on the opposite side with the same properties, keeping the number of atoms consistent throughout the simulation. The computational cost increases with the number of atoms and by applying PBCs the number of atoms needed in a simulation effectively can be reduced. If PBCs are applied in all three dimensions, the original cell is effectively simulated as a bulk material without any surface. In the same way a surface can be simulated by applying the PBCs in only two dimensions and a nanowire with PBCs in one dimension. There are, however, some risks associated with the usage of PBCs. If the simulation cell is too small long-ranged potentials can make atoms interact with themselves through the virtual cells. In high energy irradiation simulations the heat created by the ion can travel through the cell and overlap with itself if the

original cell is not large enough.

There are several different ensembles in which the system can be simulated. Inside a NVE ensemble, the total energy is conserved and atomic interactions are correctly simulated. The temperature and pressure of the system is controlled in NVT and NPT ensembles, respectively. Different parts of the system can also be simulated in different ensembles and a combination of NVE and NVT are often used to maintain a constant temperature. The thermostat is applied on the border atoms whereas a NVE ensemble is used in the center of the simulation cell to correctly simulate the atomic interactions without any scaling.

The temperature of the system can be calculated from the velocities of the particles in the system at any point in time (t) with

$$T(t) = \frac{1}{k_B N_f} \sum_i^N m_i \mathbf{v}_i^2(t) \tag{4.8}$$

where k_B is the Boltzmann constant, N_f is the number of degrees of freedom, N is the number of particles, m_i is the mass of particle i and $\mathbf{v}_i$ is the velocity of the particle. The temperature of the system is therefore controlled by scaling the velocities and hence the kinetic energy of the atoms. For its simplicity to implement the Berendsen thermostat [86] is widely used. The temperature with a Berendsen thermostat is scaled with

$$\frac{dT}{dt} = \frac{T_0 - T}{\tau} \tag{4.9}$$

where T is the temperature of the system, T_0 is the target temperature and τ is a user defined time constant. The system is coupled with an external heat bath and the time constant, τ, determines the strength of the coupling and therefore how aggressively the thermostat is applied on the system. The Berendsen thermostat fails, however, to produce a correct canonical ensemble and can produce unphysical artifacts like the flying ice cube [87]. The Nosé-Hoover thermostat [88, 89] is another temperature control, which uses a virtual extended system of particles acting as a heat reservoir. This method produces a correct canonical ensemble but the temperature fluctuations can be large when the system tries to find an equilibrium. Therefore, it is recommended to use the Berendsen thermostat until the system has reached equilibrium before switching to the Nosé-Hoover thermostat. Barostats can be applied in a similar way to control the pressure of the system and both Berendesen and Nosé-Hoover have their own widely used barostats.

Atoms are considered as point particles in MD and electrons are not explicitly included in the simulations. Therefore, the electronic stopping power is simulated by an artificial friction force, which is applied on all particles in the system with a kinetic energy above a user defined threshold.

4.2   Creation of simulation cell

The sputtering yields are studied on tungsten surfaces with several different crystal orientations, which are created similarly as presented in Refs. [24, 25, 67]. The crystalline cells are created by first building a $(0\,0\,1)$ oriented BCC cell with a $3.152\,\text{Å}$ lattice constant, which corresponds to the lattice constant at $300\,\text{K}$ with the Marinica *et al.* EAM potential [90] with corrections by Sand *et al.* [91]. To get the desired crystal direction, the cell is then rotated with the Euler angles α_E, β_E and γ_E.

The amorphous cell is created by first making a $40\,\text{Å} \times 40\,\text{Å} \times 40\,\text{Å}$ simulation cell containing 4088 randomly placed tungsten atoms. The cell is then heated up to $10\,000\,\text{K}$ before quenched down to $300\,\text{K}$ at the rate of $0.01\,\text{K/fs}$ with PBCs applied in all dimensions. The quench is followed by a $100\,\text{ps}$ simulation at $300\,\text{K}$ to relax the system. The cell was further simulated at $300\,\text{K}$ in a NPT ensemble for $200\,\text{ps}$ with the Berendsen thermostat and barostat applied. The cell could hence expand and get rid of the excess pressure that had built up in it. The cell is then duplicated in all three dimensions to get the required cell size.
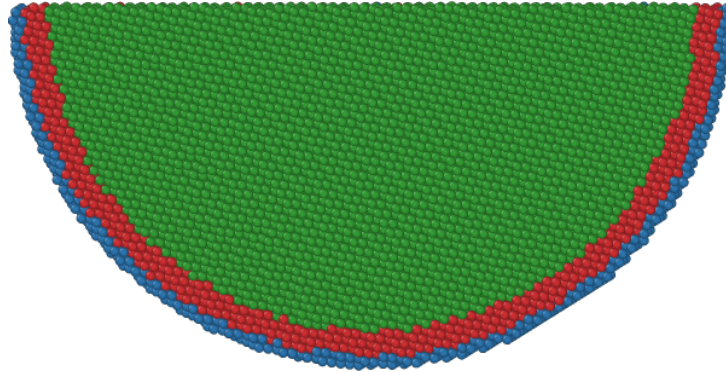

Figure 4.3: In the simulation cell, the green atoms are in the NVE ensemble, the red atoms in the NVT ensemble and the blue atoms are fixed in position to prevent the cell from moving.

Both the crystalline and amorphous simulation cells are then cut into hemispheres with the radius $r_s = 80\,\text{Å}$ for the $1.5\,\text{keV}$ simulations and $r_s = 100\,\text{Å}$ for both the $5\,\text{keV}$ and $7.5\,\text{keV}$ irradiation simulations. The hemispheres consist of three different radial layers, which are visualized in Fig. 4.3. The innermost layer, from the center of the hemisphere to $r_s - 10$ Å, is in the NVE ensemble to accurately conserve the energy and handle the many-body collisions caused by the primary knock-on atom. Atoms in the next layer, $[r_s - 10$ Å, $r_s - 3$ Å$]$, are controlled by the Berendsen thermostat and their velocities are scaled to get rid of the excess energy. In the outermost region, $[r_s - 3$ Å, $r_s]$, are the atoms fixed in position to prevent the cell from moving. To thermalize the system and relax the surface the cell is simulated for $10\,\text{ps}$ at $300\,\text{K}$.

4.3 Irradiation simulations

The molecular dynamics code PARCAS [66] is used in the irradiation simulations and the W-W interactions are handled by the same Marinica interatomic potential [90,91] that is used in the simulation cell creation. Instead of bombarding the surface with ions, the irradiation is carried out with the primary knock-on atom (PKA) method. The kinetic energy is given to an already existing atom in the system, which acts as if it had been hit by an ion and starts a collision cascade. Therefore, sputtering from all surface orientations can be compared with the irradiation energy equally deposited in the near surface layers. This gave consistent results as the energy is dispersed at roughly the same position and depth every time. Therefore, fewer simulations are needed to gather good statistics as every simulation is a direct hit. Furthermore, this allows for faster simulations as smaller systems and lower irradiation energies are required.

The angle of incidence is determined by the polar angle θ and the azimuthal angle ϕ, visualized in Fig. 4.4. The polar angle is chosen from the interval $[0°, 180°]$ with $0°$ being in the positive z-direction and $180°$ in the negative z-direction. In these simulations the polar angle is chosen at random between $140°$ and $180°$. Therefore, the PKA has a kinetic energy in a direction between $0°$ and $40°$ off-normal downwards. The azimuthal angle is chosen at random and rotates around the z-axis.

The irradiation simulations are done in two different series. In the first one is the PKA at the surface and for the other one is it at a 1 nm depth. The surface
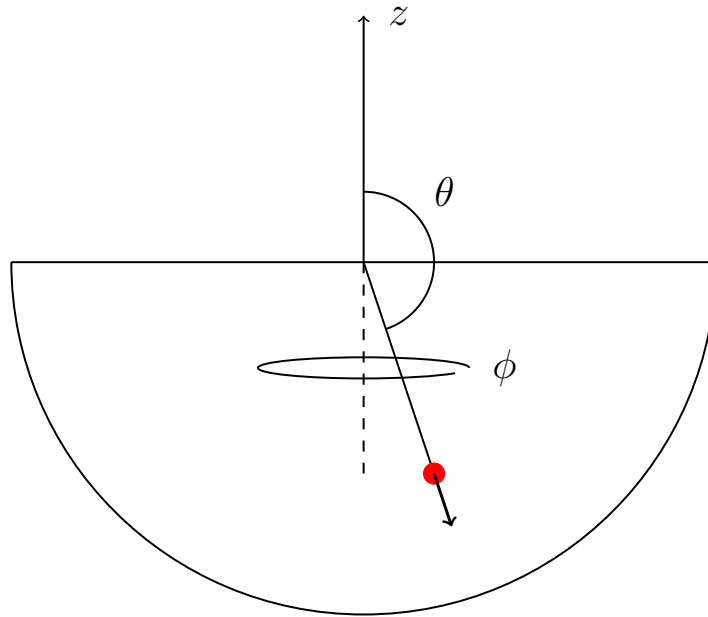

Figure 4.4: The polar angle θ and azimuthal angle ϕ

series is a reference study for normal ion bombardment were the ion hits the surface and disperse its energy there. The other one simulates a situation where the ion penetrates the first few surface layers and disposes most of it's energy deeper within the material. The PKA is chosen at random from a $6\,\text{Å} \times 6\,\text{Å}$ square centered on the circular surface or at a depth of $1\,\text{nm}$. The irradiation energies for the PKA in the simulations are $1.5\,\text{keV}$, $5\,\text{keV}$ and $7.5\,\text{keV}$, and the studied surface orientations are $(0\,0\,1)$, $(0\,1\,1)$, $(0\,1\,2)$, $(1\,1\,1)$, $(3\,1\,5)$, $(3\,1\,9)$ and an amorphous surface. For the $1.5\,\text{keV}$ simulations, two additional surface orientations are investigated, $(1\,1\,3)$ and $(2\,1\,3)$. Therefore, a total of 18 individual simulation cases are required for $1.5\,\text{keV}$ and 14 cases for $5\,\text{keV}$ and $7.5\,\text{keV}$.

For every surface orientation and energy, at least 1 900 irradiation simulations were carried out on a pristine surface at $300\,\text{K}$ for $10\,\text{ps}$. To get rid of the excess heat in the system, the Berendsen thermostat is applied on atoms in the same region as described in the previous section. Electronic stopping is applied as a friction force on all atoms in the system with a kinetic energy above $5\,\text{eV}$.

4.4 Analysis

The sputtering yield and angular distribution from several surface orientations are studied and compared by different methods. For visualizing the results, the open visualization tool OVITO [92] is used. The program has several built-in modifiers, which help to analyze the cascade evolution in the system. The radius of the hemisphere was large enough for the cascade to stay within the NVE ensemble. Therefore, no sputtering was occurring from cascades reflecting back from the fixed atoms in the outermost layer.

The interatomic potential has a cut-off distance of 5.5 Å, which determines the longest distance atoms can be from each other while still interacting. If an atom is further than 5.5 Å from the surface of the system it does not feel an attractive force towards it anymore. Therefore, the number of sputtered atoms can in each simulation be counted using the cut-off distance. The method checks at the end of every simulation if any atoms are above the cut-off distance from the surface and marks them as sputtered. Although some atoms may have momentarily left the surface during the simulation can they return to the surface if they stayed within the cut-off distance and are therefore not counted as sputtered. The other implemented method checks for cluster formation on the surface. For an atom to be counted as sputtered it cannot be in contact with any atoms still connected to the surface. This is, however, unlikely with the bombardment energies in these simulations and the two methods were in excellent agreement with each other.

Once the number of sputtered atoms is known for every simulation, the sputtering yield is calculated for all surfaces according to the formulae in Eq. (2.1). Additionally to the total sputtering yield, the angular distribution of the sputtered atoms is studied. The outgoing angle for every sputtered atom is calculated with their velocity components. The outgoing angle, α, is therefore calculated with

$$\alpha = \tan^{-1}\left(\frac{\sqrt{\mathbf{v}_x^2 + \mathbf{v}_y^2}}{\sqrt{\mathbf{v}_z^2}}\right) \qquad (4.10)$$

where $\mathbf{v}_x$, $\mathbf{v}_y$ and $\mathbf{v}_z$ are the velocity components in the x-, y- and z-directions. The outgoing angle of the sputtered atom is defined by having 0° perpendicular to the surface and 90° in parallel with it. The interval of the outgoing angles $[0°, 90°]$ is further divided into 20 bins, with each being 4.5° wide. The sputtering yield is then calculated for each bin by dividing the number of sputtered atoms in the outgoing angle with the total number of PKAs introduced in the system.

Collision cascades can effectively propagate in the most close packed and other highly symmetrical directions. The angle between these crystal directions and the

surface orientation is therefore investigated. The angle between two crystal directions is calculated by Eq. (4.11)

$$\cos\left(\phi\right) = \frac{h_1 h_2 + k_1 k_2 + l_1 l_2}{\sqrt{h_1^2 + k_1^2 + l_1^2}\sqrt{h_2^2 + k_2^2 + l_2^2}} \tag{4.11}$$

where ϕ is the angle between two surface directions, h_1, k_1, l_1 and h_2, k_2, l_2 are the Miller indices for the first and second crystal direction, respectively. For tungsten, which is a BCC material, $\langle 1\,1\,1 \rangle$ is the most close packed direction. The formulae can therefore be simplified to

$$\phi = \cos^{-1}\left(\frac{1}{\sqrt{3}} \frac{h + k + l}{\sqrt{h^2 + k^2 + l^2}}\right) \tag{4.12}$$

and for the highly symmetrical $\langle 0\,0\,1 \rangle$ direction

$$\phi = \cos^{-1}\left(\frac{l}{\sqrt{h^2 + k^2 + l^2}}\right) \tag{4.13}$$

were h, k and l are the Miller indices of the other crystal direction.

The errors in the sputtering yield for each surface orientation is estimated with the standard error of the mean, Eq. (4.14). The error of the total sputtering yield for a surface orientation is therefore

$$\sigma_{\overline{x}} = \frac{\sqrt{\sum_{i=1}^{N}\left(x_i - \overline{x}\right)^2}}{N} \tag{4.14}$$

where $\sigma_{\overline{x}}$ is the estimated error, $\overline{x}$ is the total sputtering yield for a surface orientation, x_i the number of sputtered atoms in every individual simulation and N the number of individual simulations in the series.

5. Results

5.1 Simulated sputtering yields

In this section we will go through the total sputtering yields from the primary knock-on (PKA) simulations. During ion irradiation, the sputtering yield does depend on the nature of the collision between the incoming ion and a surface atom. The advantage for using the PKA method is the equal energy deposition for each simulation and between every surface orientation. In this way, different surface orientations are all compared to each other as if the energy was deposited equally in the top surface layers. The energy is not equally disposed between different surface orientations in experiments but is, however, a useful tool in these simulations for studying the behavior and similarities between them.

The sputtering yields for all surface orientations and energies are presented in Tab. 5.1 with a more visual representation in Fig. 5.1. From the results it can be seen how strongly the sputtering yields depend on the initial energy. When the PKA is on the surface, the (1 1 1) surface has the highest sputtering yield of all crystalline surfaces and the amorphous surface has generally the lowest. When the energy is increased to 5 keV and 7.5 keV the surface orientations can be categorized
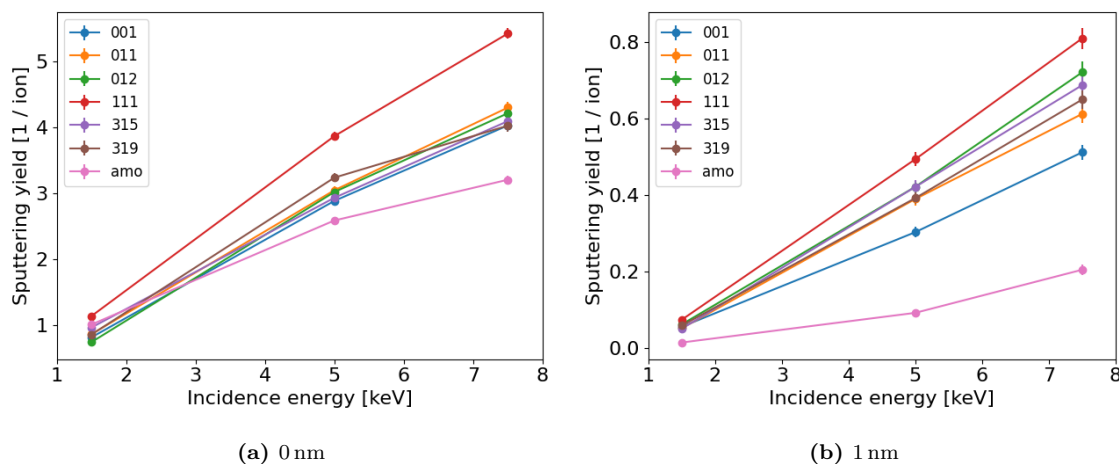

(a) 0 nm   **(b)** 1 nm

Figure 5.1: The sputtering yields for all surface orientations

into three distinct groups. The (1 1 1) surface continues with the highest sputtering yield, the amorphous material has the lowest and the rest of the surface orientations have sputtering yields relatively close to each other. When the energy is dispersed at 1 nm the (1 1 1) surface has still the highest sputtering yield. The difference between the crystalline surfaces and the amorphous has increased and the sputtering yield is up to several factors lower for the amorphous surface. The sputtering yield of the (0 0 1) surface has become noticeably lower than the rest of the crystalline surfaces, which are still relatively close to each other, even in the higher energy cases.

Surface orientation	Sputtering yield [1/ion]		
	1.5 keV	5 keV	7.5 keV
(0 0 1)	0.81 ± 0.02	2.88 ± 0.05	4.03 ± 0.06
(0 1 1)	0.86 ± 0.02	3.05 ± 0.07	4.30 ± 0.08
(0 1 2)	0.74 ± 0.02	3.02 ± 0.06	4.21 ± 0.09
(1 1 1)	1.14 ± 0.02	3.87 ± 0.07	5.42 ± 0.08
(1 1 3)	0.96 ± 0.02		
(2 1 3)	0.90 ± 0.02		
(3 1 5)	0.96 ± 0.02	2.93 ± 0.06	4.09 ± 0.07
(3 1 9)	0.85 ± 0.02	3.24 ± 0.06	4.03 ± 0.09
amorphous	1.01 ± 0.02	2.59 ± 0.05	3.21 ± 0.07

(a) Sputtering yields for all surface orientations for the primary knock-on atom at the surface

Surface orientation	Sputtering yield [1/ion]		
	1.5 keV	5 keV	7.5 keV
(0 0 1)	0.055 ± 0.004	0.30 ± 0.01	0.51 ± 0.02
(0 1 1)	0.051 ± 0.004	0.39 ± 0.02	0.61 ± 0.02
(0 1 2)	0.061 ± 0.005	0.42 ± 0.02	0.72 ± 0.03
(1 1 1)	0.074 ± 0.005	0.49 ± 0.02	0.81 ± 0.03
(1 1 3)	0.047 ± 0.004		
(2 1 3)	0.063 ± 0.004		
(3 1 5)	0.050 ± 0.004	0.42 ± 0.02	0.69 ± 0.03
(3 1 9)	0.058 ± 0.004	0.39 ± 0.01	0.65 ± 0.02
amorphous	0.014 ± 0.002	0.09 ± 0.01	0.20 ± 0.01

(b) Sputtering yields for all surface orientations for the primary knock-on atom at 1 nm depth

Table 5.1: Sputtering yields from all surface orientations. The results are for the initial energies 1.5 keV, 5 keV and 7.5 keV acting on the primary knock-on atom (a) at the surface and (b) at the depth of 1 nm. The errors are calculated with the standard error of the mean.

Some crystal directions are more pronounced to channeling as seen in channeling maps [23, 25, 38], which can decrease the sputtering yield by several orders of magnitude [39, 40]. Channeling between an ion and the material cannot occur in these simulations because of the PKA method and the energy is equally disposed for every surface orientation. Therefore, these sputtering yields are not directly comparable to ion irradiation experiments. For instance, the $(1\,1\,1)$ surface has the highest sputtering yield in these simulations although it is a strong channeling direction. Only a small amount of the bombardment energy is usually deposited in the near surface layers, as seen in Fig. 3.1, and the $(1\,1\,1)$ surface has typically a low sputtering yield.

The surface binding energy is directly proportional to the atom density on the surface [11]. Different surface orientations have different surface morphology, as seen in Fig. 5.2, and less kinetic energy is needed for edge atoms and atoms from steps to sputter compared to surface atoms on denser and smoother surfaces [32]. For more dense surfaces is it harder for the ion to penetrate the surface layer but a collision with a surface atom is more probable. It is easier for single knock-on sputtering to occur for less dense surfaces but the atom may travel deep into the material before colliding with an atom. This effect is again not present in the PKA method because the irradiation energy is deposited equally for every surface orientation and does not depend on an initial collision between the ion and a surface atom.
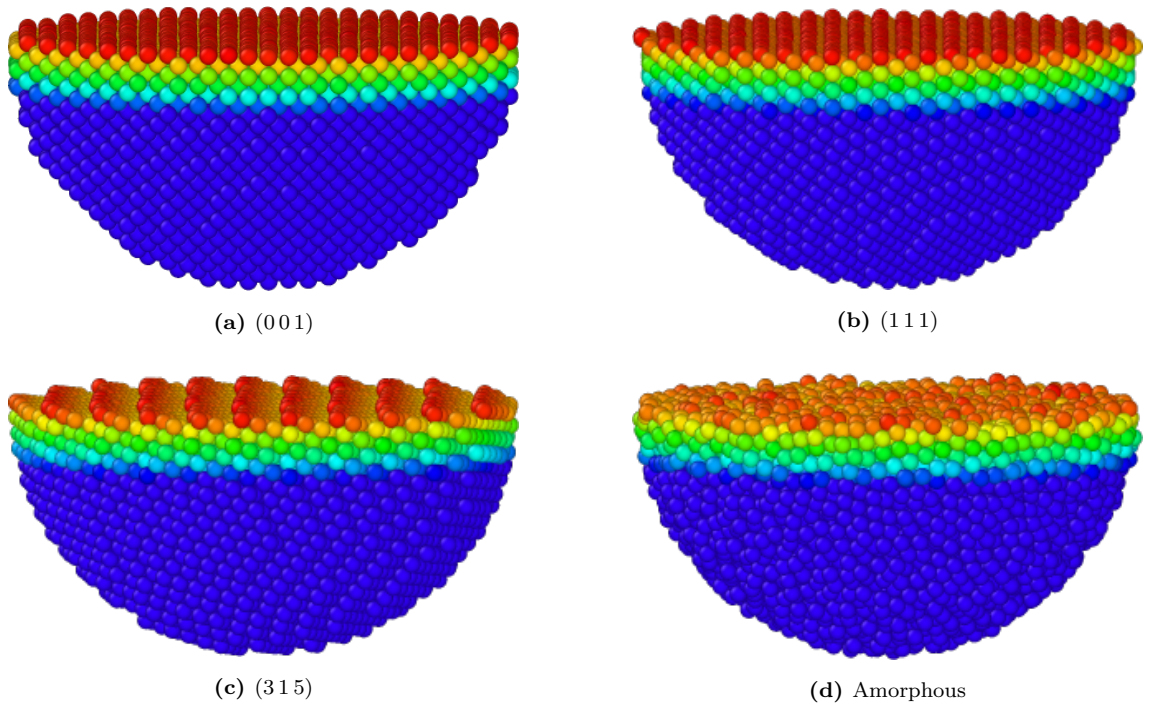

(a) $(0\,0\,1)$

(b) $(1\,1\,1)$

(c) $(3\,1\,5)$

(d) Amorphous

Figure 5.2: The surface morphology of different surface orientations

5.2 Angular distribution of sputtered atoms

Additionally to the total sputtering yield, the angular distribution of the sputtered atoms is studied. The outgoing angles are divided into bins with 4.5° intervals with the corresponding sputtering yield plotted in the center of every bin, see Fig. 5.4. The outgoing angle is defined as the angle between the trajectory of the sputtered atom and the surface normal.

In the first case, where the PKA is on the surface, the angular distribution is relatively similar for all surface orientations. The sputtering occurs mainly in angles in the center of the distribution with little sputtering occurring at the lowest and highest angles. The whole distribution is also a little shifted toward lower angles. The exceptions are the (0 0 1) and (1 1 1) surfaces, where sputtering occurs mainly outside the main trend. Additionally to the broader distributions, these surface orientations have two peaks unlike all other surface orientations, which only have one peak. The (0 1 1) surface orientation has a narrower distribution than the rest of the surface orientations with almost all of the sputtering occurring around 45°. For normal incidence ion irradiation polycrystalline and amorphous surfaces are described by a cosine shaped angular distribution [27, 32]. Although only a few different surface orientations are studied in this thesis, they are averaged into a single distribution, which represents a polycrystalline surface. When comparing the shapes of the averaged and amorphous distributions in Fig. 5.3 are they both similar and somewhat cosine shaped, which in good agreement with the original assumption.

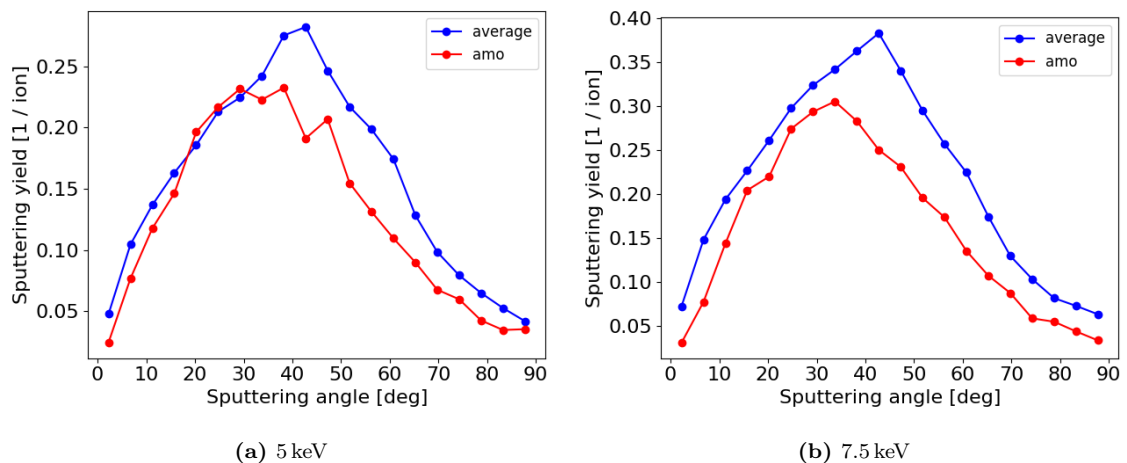In the second case where the energy is disposed at 1 nm depth the distributions

(a) 5 keV   **(b)** 7.5 keV

Figure 5.3: Angular distributions for the averaged sputtering yield of all crystalline surfaces and the amorphous surface with the PKA on the surface

(a) 1.5 keV

(b) 1.5 keV

(c) 5 keV

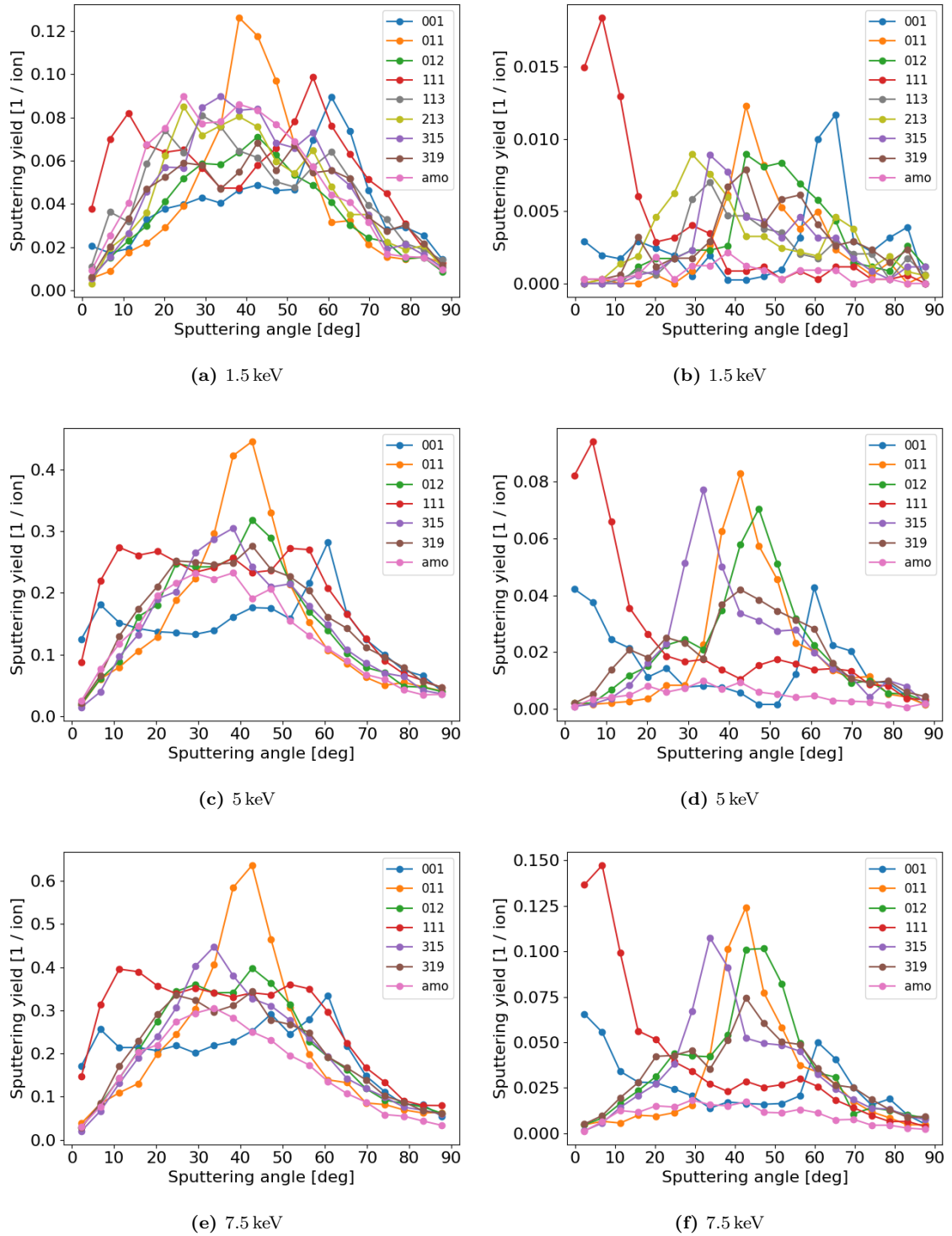**(d)** 5 keV

(e) 7.5 keV

(f) 7.5 keV

Figure 5.4: The sputtering yields as a function of the angle of the sputtered atoms. The outgoing angles are divided by 4.5° into bins with the corresponding sputtering yield in the center. The graphs on the left side (a),(c) and (e) has the primary knock-on atom at the surface and the graphs on the right side (b), (d) and (f) has the primary knock-on atom at the depth of 1 nm. The specific sputtering angles for each crystalline surface orientation can be seen as peaks in the graphs whereas the peaks are absent for the amorphous surface.

are different. Unlike in the fist case where the angular distributions were cosine shaped most of the sputtering is now occurring in specific outgoing angles. When the PKA energy is increased to 5 keV and 7.5 keV the specific outgoing angles are more pronounced. The sputtering yield is generally up to several factors higher at the peaks compared to the rest of the outgoing angles in the distribution. Throughout all bombardment energies, the (0 0 1) surface has two peaks instead of only one, unlike the the rest of the surface orientations, located around 0° and 60°. Most of the atoms are sputtering in 60° off surface normal for 1.5 keV irradiation. When the energy is increased, more sputtering is occurring at 0° instead and the sputtering is equally divided between the two peaks at 5 keV. When the energy is further increased to 7.5 keV the sputtering has shifted to mainly occur at 0°.
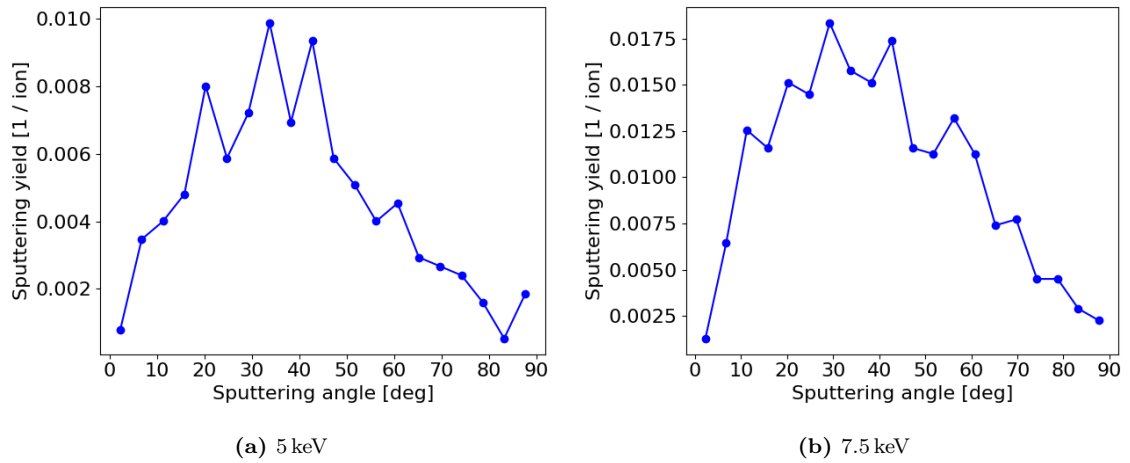

(a) 5 keV   **(b)** 7.5 keV

Figure 5.5: Angular distribution of the amorphous material with the PKA at 1 nm depth

The total sputtering yields are generally lower for the amorphous surfaces compared to the crystalline surfaces, as discussed in the previous section. This trend can also be seen in Fig. 5.3, as the sputtering yield of the amorphous distributions are generally lower than in the angular distributions of the crystalline surfaces. The amorphous surfaces have also a more cosine shaped distribution when the PKA is at 1 nm depth as seen in Fig. 5.5. The peaks in the angular distributions, which are characteristic for the crystalline materials, are absent for the amorphous surfaces. Hence one can conclude that except for the cosine distribution the amorphous surface has no specific outgoing angles in which the atoms would sputter more frequently.

5.3 Underlying mechanisms for angular distribution

Every crystalline surface orientation has a specific angle in which the atoms prefer to sputter when the energy is disposed at 1 nm depth, as seen in the previous section. Linear collision sequences can efficiently propagate through materials in the most close packed direction. For a BCC material like tungsten, the $\langle 1\,1\,1 \rangle$ direction is most close packed. Therefore, the angle between the surface normal and the $\langle 1\,1\,1 \rangle$ direction is calculated for every surface orientation with Eq. 4.11. The calculated angles, presented in Tab. 5.2, are in good agreement with the peaks in the angular distributions, which are visualized for a couple of surface orientations in Fig. 5.6. The simulated peaks are, however, at slightly higher angles compared to the theoretical ones. The overestimation for the simulated peak angles are likely due to the attractive force from the surface. As a sputtered atom leaves the surface is it affected by the interatomic potential and dragged towards it, which increases the sputtering angle.

By arranging the total sputtering yield as a function of the peak angle, the correlation between them is clear in the results, Fig. 5.9. When the PKA is at 1 nm depth the total sputtering yield is heavily influenced by the angle between the surface direction and the $\langle 1\,1\,1 \rangle$ direction. The $(1\,1\,1)$ surface has the highest sputtering
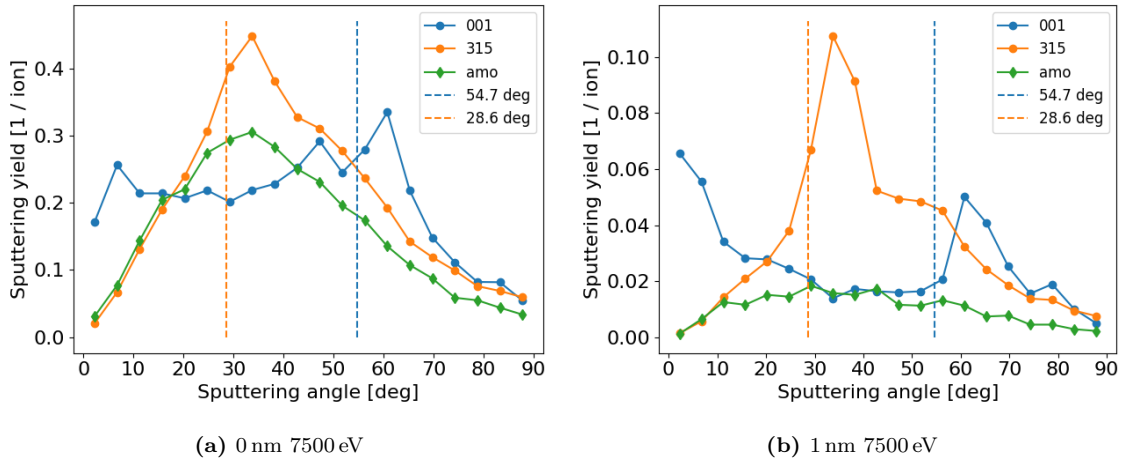

(a) 0 nm 7500 eV

(b) 1 nm 7500 eV

Figure 5.6: The simulated peak angles in the distribution compared to the theoretical angle for the $(0\,0\,1)$, $(3\,1\,5)$ and amorphous surface

$\langle 0\,0\,1 \rangle$	$\langle 0\,1\,1 \rangle$	$\langle 0\,1\,2 \rangle$	$\langle 1\,1\,1 \rangle$	$\langle 1\,1\,3 \rangle$	$\langle 2\,1\,3 \rangle$	$\langle 3\,1\,5 \rangle$	$\langle 3\,1\,9 \rangle$
54.7°	35.3°	39.2°	0.0°	29.5°	22.2°	28.6°	38.1°

Table 5.2: The angles between the surface normal and the most close packed $\langle 1\,1\,1 \rangle$ direction.

yield as the distance from the PKA to the surface is the shortest. The distance the linear collision cascade has to travel towards the surface in the $\langle 1\,1\,1 \rangle$ direction increases when the angle between the surface normal and the $\langle 1\,1\,1 \rangle$ direction gets higher. For all crystalline surface orientations, the sputtering yield is decreasing with increasing peak angles. The collision sequence has to travel a longer distance inside the material and the probability for the cascade to reach the surface with enough energy to cause an atom to sputter decreases with distance. Therefore, the sputtering yield is decreasing with increasing peak angles, as seen in Fig. 5.9. The surface orientations with peak angles close to each other have similar sputtering yields but the $(0\,0\,1)$ surface, which has the highest peak angle of all crystalline surfaces, has clearly the lowest sputtering yield of them all.

Atoms in the linear collision sequence are moving in the $\langle 1\,1\,1 \rangle$ row in a sequence of collisions as shown in Fig. 5.7 and Fig. 5.8 for the $(0\,0\,1)$ and $(3\,1\,5)$ surfaces, respectively. The linear collision sequences in these figures have their origin at almost $2\,\mathrm{nm}$ depths and travel thorough several atom layers before reaching the surface. Therefore, sputtering can occur from cascades propagating from deeper within the material and not only from collisions in the top surface layers.
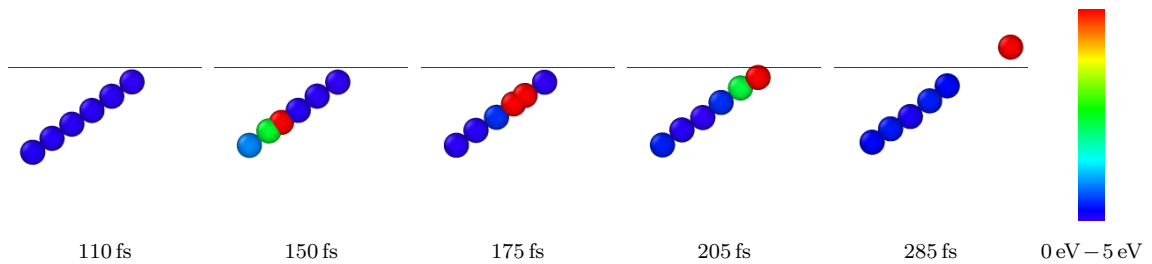

| 110 fs | 150 fs | 175 fs | 205 fs | 285 fs | $0\,\mathrm{eV} - 5\,\mathrm{eV}$ |

Figure 5.7: A linear collision sequence in the $\langle 1\,1\,1 \rangle$ direction for a $(0\,0\,1)$ surface.

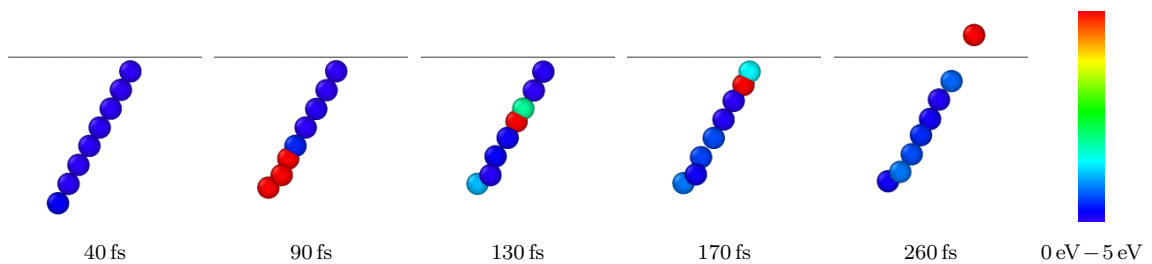| 40 fs | 90 fs | 130 fs | 170 fs | 260 fs | $0\,\mathrm{eV} - 5\,\mathrm{eV}$ |

Figure 5.8: A linear collision sequence in the $\langle 1\,1\,1 \rangle$ direction for a $(3\,1\,5)$ surface.

The effect is less pronounced when the PKA is at the surface. In the higher energy cases, all crystalline surface orientations except the $(1\,1\,1)$ surface have relatively similar sputtering yields. The sputtering yields of the $(0\,0\,1)$ surface is hence more similar to the rest of the crystalline surface orientations unlike when the PKA

(a) 1.5 keV

(b) 1.5 keV

(c) 5 keV

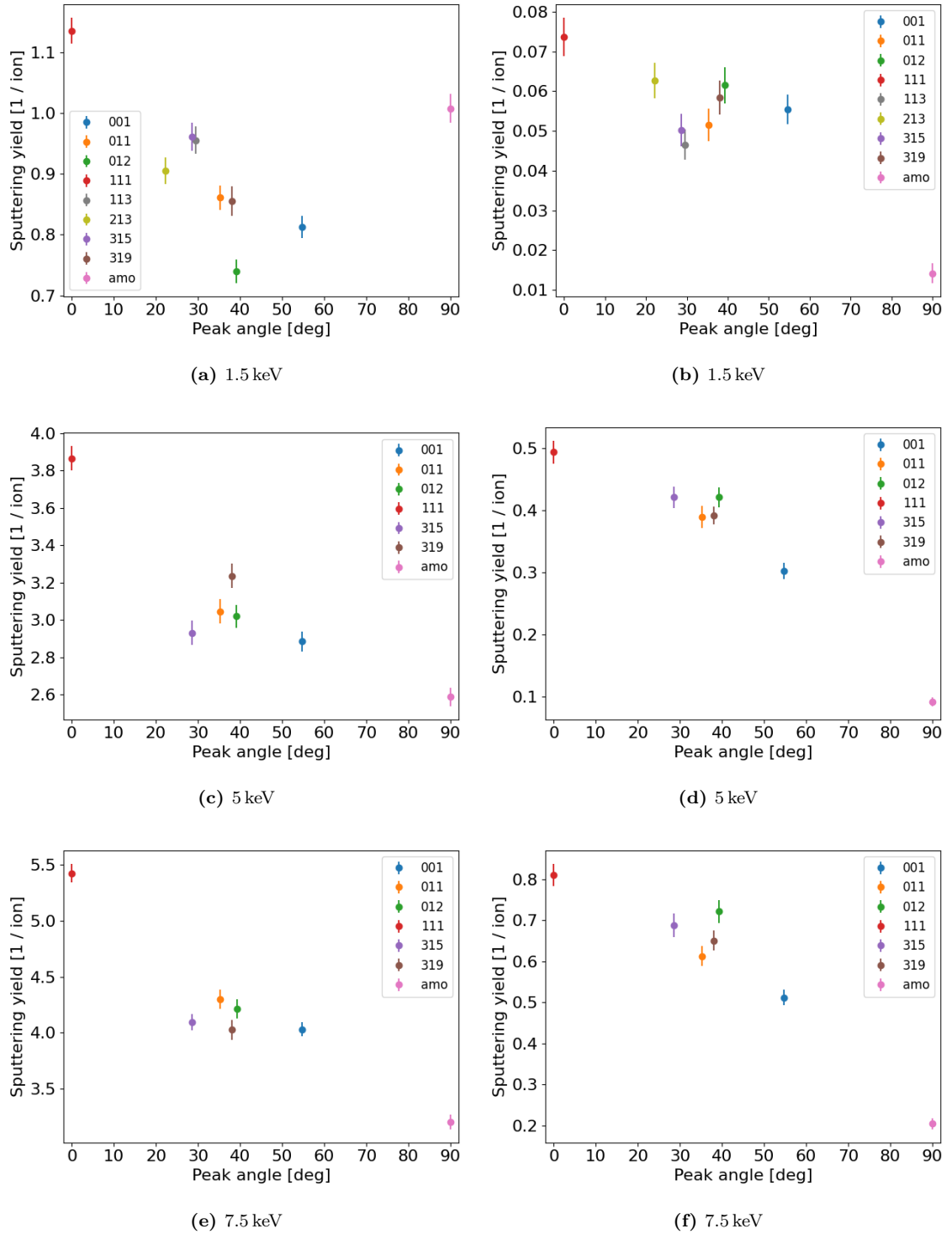**(d)** 5 keV

(e) 7.5 keV

(f) 7.5 keV

Figure 5.9: Total sputtering yields versus the peak angle for each surface orientation. The placement for the amorphous surface is arbitrary. The PKA is placed on the surface for (a), (c) and (e) and at 1 nm depth for (b), (d) and (f). Surface orientations with larger angles between the surface normal and the ⟨1 1 1⟩ direction have lower sputtering yields. The amorphous surface, which has no peak angle, has a significantly lower sputtering yields than the crystalline surfaces.

was at 1 nm depth. Although most of the studied crystalline surface orientations have their calculated peak angles in the center of the angular distribution, the angular distribution is broader and cosine shaped. This indicates that linear collision sequences in the $\langle 1\,1\,1 \rangle$ direction is not as important as when the PKA was at 1 nm depth. The low sputtering yields for the amorphous surfaces in the 5 keV and 7.5 keV simulations still show, however, that the crystalline surfaces are able to transport the recoil energy more efficiently.

The $(0\,0\,1)$ surface is the only surface orientation which has two distinct peaks when the PKA is at 1 nm. The theoretical peak is at 54.7°, which corresponds well with the results, and the second peak has it's maximum at around 0°. The $\langle 0\,0\,1 \rangle$ direction is a symmetrical next-nearest neighbor direction and sputtering in this outgoing angle is hence a possible reason to the high sputtering yield around 0°. The collision cascade has to travel a long distance in the material when the angle between the surface normal and the $\langle 1\,1\,1 \rangle$ direction is high to reach the surface. The distance for the cascade to travel in the $\langle 0\,0\,1 \rangle$ direction is much shorter and hence this might be the reason for the sputtering yields of the two peaks to be so close to each other. The atoms in the sequence have, however, to push through the $(0\,0\,1)$ plane, which might explain why sputtering in this direction was only favourable in the 5 keV and 7.5 keV cases. A linear collision sequence for the $(0\,0\,1)$ surface in the $\langle 0\,0\,1 \rangle$ direction is illustrated in Fig. 5.10.
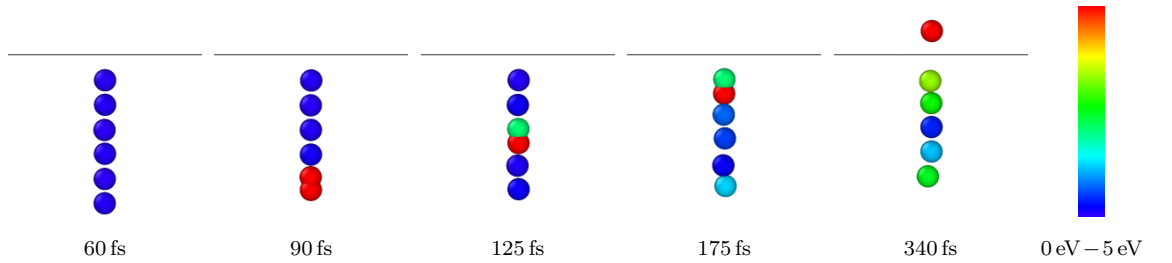

60 fs	90 fs	125 fs	175 fs	340 fs	0 eV − 5 eV

Figure 5.10: Linear collision sequence in the next-nearest neighbor $\langle 0\,0\,1 \rangle$ direction for a $(0\,0\,1)$ surface.

For all crystalline surface orientations, there is a contribution to the sputtering yield in the $\langle 0\,0\,1 \rangle$ direction. The contribution is not as strong as from the $\langle 1\,1\,1 \rangle$ direction and mainly noticeable in the angular distributions of the $(0\,0\,1)$ and $(1\,1\,1)$ surfaces. For some surface orientations the two sputtering angles are close to each

$\langle 0\,0\,1 \rangle$	$\langle 0\,1\,1 \rangle$	$\langle 0\,1\,2 \rangle$	$\langle 1\,1\,1 \rangle$	$\langle 1\,1\,3 \rangle$	$\langle 2\,1\,3 \rangle$	$\langle 3\,1\,5 \rangle$	$\langle 3\,1\,9 \rangle$
0.0°	45.0°	26.6°	54.7°	25.2°	36.7°	32.3°	19.4°

Table 5.3: The angles between the surface normal and the $\langle 0\,0\,1 \rangle$ direction.

other, which results in overlaps in the angular distribution in Fig. 5.4. For the $(0\,1\,1)$ surface both the $\langle 1\,1\,1 \rangle$ and $\langle 0\,0\,1 \rangle$ directions are in a 45° angle from the surface normal. This could explain why the angular distribution for the $(0\,1\,1)$ surface was so much narrower compared to the other surface orientations and only concentrated around 45°. Emission patterns in the $\langle 1\,0\,0 \rangle$ direction for both BCC and FCC single crystalline surfaces has also experimentally been observed [49].

Except for the differences in the sputtering yield between the crystalline surfaces, also the large difference between them and the amorphous surface can be explained. The absence of an ordered structure for the amorphous surface makes it impossible for linear collision cascades to travel in a close packed direction all the way to the surface and the sputtering yield is hence much lower. As seen in the angular distribution for the crystalline surfaces in Fig. 5.4 the majority of sputtering occurs around these peak angles and the sputtering yield is much lower elsewhere in the distribution. Without this process, which contributes to almost all of to the total sputtering yield, the sputtering yield is much lower for the amorphous surface when the energy is deposited equally in the material.

6. Conclusions

The amount of energy deposited in the topmost surface layers is shown to have large effect on the sputtering yield. For low-index surfaces, the ion can penetrate deep into the material trough channels in the material and deposit it's energy there. High-index surfaces with no channeling have large amounts of recoil energy in the topmost surface layers. The correlation between the sputtering yield and the energy given to recoils in the surface layers is shown to have a linear dependency [23]. In this thesis, the sputtering yields of several different surface orientations are studied using the primary knock-on atom method. By using this method the energy is deposited equally for every surface orientation and the recoil energy is therefore the same for every orientation. Hence, every surface orientation investigation is independent of the surface morphology.

The results show that linear collision sequences play a significant role in the process of sputtering and in the underlying mechanism leading to a specific pattern of the outgoing angle of sputtered atoms. The recoils are propagating in the most close packed direction, the $\langle 1\,1\,1 \rangle$ direction, in linear collision sequences and can therefore efficiently transport the energy through the material. The phenomenon is more pronounced when the PKA is placed $1\,\mathrm{nm}$ beneath the surface and leads to a peak in the angular distributions for every surface orientation. The peak in the distribution is located at the same angle as the angle between the surface normal and $\langle 1\,1\,1 \rangle$ direction. As the angle between the surface normal and the $\langle 1\,1\,1 \rangle$ direction increases, the recoils in the sequence have a longer distance to travel in the material before the energy reaches the surface atom. Therefore, the total sputtering yield is lower for surface orientations with high peak angles when the energy is deposited equally inside the material. Sputtering in another highly symmetrical direction, the $\langle 0\,0\,1 \rangle$ direction, also contributes to the total sputtering yield. For surface orientations with high peak angles, sputtering in the $\langle 0\,0\,1 \rangle$ direction can be favourable at higher incidence energies, which leads to sputtering in this next-nearest neighbor direction as well.

Amorphous materials do not have a crystal structure and hence no long term order in the material. Ions cannot therefore move through rows and open paths in

the material, and the bombardment energy is deposited in the near surface layers. Furthermore, linear collision sequences are an important sputtering mechanism for crystalline materials and the main source of sputtering when the energy is dispersed inside the material. The absence of long range order in the amorphous material makes it impossible for linear collision sequences to efficiently propagate through the material. Therefore, the sputtering yield is significantly lower for the amorphous surface compared to crystalline surfaces under equal deposited energy conditions.

Amorphous and polycrystalline materials have both a cosine shaped angular distribution when the PKA is at the surface. Linear collision sequences in polycrystalline materials lead to more sputtering in all angular directions and random surface crystal directions on the surface would likely further increase sputtering in high outgoing angles. Therefore, polycrystalline materials have a higher total sputtering yield than amorphous materials, although they both have similar angular distributions.

In the future, the method presented in this thesis could be applied on other surface orientations and materials. Most of the studied crystalline surface orientations had their peak angles close to each other and additional surface orientations could therefore extend this study and validate the findings in this thesis. Sputtering in the $\langle 1\,1\,1 \rangle$ direction is already dominant when the PKA is at $1\,\mathrm{nm}$ depth. Therefore, at which depth linear collision sequences becomes important could be investigated. Additionally, the distance linear collision sequences can travel inside the material could be studied by having the PKA at different depths.

References

[1] International Thermonuclear Experimental Reactor, ITER, https://www.iter.org.

[2] ITER, tritium breeding, https://www.iter.org/mach/tritiumbreeding, visited 27.6.2022.

[3] ITER, blanket, https://www.iter.org/mach/blanket, visited 22.1.2022.

[4] L. Giancarli, M. Abdou, D. Campbell, V. Chuyanov, M. Ahn, M. Enoeda, C. Pan, Y. Poitevin, E. R. Kumar, I. Ricapito *et al.*, "Overview of the ITER TBM Program," *Fusion Engineering and Design*, vol. 87, no. 5-6, pp. 395–402, 2012.

[5] A. M. Bradshaw, T. Hamacher, and U. Fischer, "Is nuclear fusion a sustainable energy form?" *Fusion Engineering and Design*, vol. 86, no. 9-11, pp. 2770–2773, 2011.

[6] J. Lister and H. Weisen, "What will we learn from ITER?" *europhysics news*, vol. 36, no. 2, pp. 47–51, 2005.

[7] ITER, divertor, https://www.iter.org/mach/divertor, visited 22.1.2022.

[8] M. Rieth, S. L. Dudarev, S. G. De Vicente, J. Aktaa, T. Ahlgren, S. Antusch, D. Armstrong, M. Balden, N. Baluc, M.-F. Barthe *et al.*, "Recent progress in research on tungsten materials for nuclear fusion applications in Europe," *Journal of Nuclear Materials*, vol. 432, no. 1-3, pp. 482–500, 2013.

[9] V. Philipps, "Tungsten as material for plasma-facing components in fusion devices," *Journal of nuclear materials*, vol. 415, no. 1, pp. S2–S9, 2011.

[10] M. Klimenkov, U. Jäntsch, M. Rieth, H. Schneider, D. Armstrong, J. Gibson, and S. Roberts, "Effect of neutron irradiation on the microstructure of tungsten," *Nuclear Materials and Energy*, vol. 9, pp. 480–483, 2016.

[11] G. Ran, S. Wu, X. Liu, J. Wu, N. Li, X. Zu, and L. Wang, "The effect of crystal orientation on the behavior of a polycrystalline tungsten surface under focused Ga+ ion bombardment," *Nuclear Instruments and Methods in Physics Research Section B: Beam Interactions with Materials and Atoms*, vol. 289, pp. 39–42, 2012.

[12] Y. Noiri, S. Kajita, and N. Ohno, "Nanostructure growth by helium plasma irradiation to tungsten in sputtering regime," *Journal of Nuclear Materials*, vol. 463, pp. 285–288, 2015.

[13] T. H. Kwon, S. Park, J. M. Ha, and Y.-S. Youn, "Study on sputtering yield of tungsten with different particle sizes: Surface roughness dependence," *Nuclear Engineering and Technology*, vol. 53, no. 6, pp. 1939–1941, 2021.

[14] E. Hechtl, H. Yang, C. Wu, and W. Eckstein, "An experimental study of tungsten self sputtering," *Journal of nuclear materials*, vol. 176, pp. 874–876, 1990.

[15] G. Van Rooij, J. Coenen, L. Aho-Mantila, S. Brezinsek, M. Clever, R. Dux, M. Groth, K. Krieger, S. Marsen, G. Matthews *et al.*, "Tungsten divertor erosion in all metal devices: Lessons from the ITER like wall of JET," *Journal of Nuclear Materials*, vol. 438, pp. S42–S47, 2013.

[16] W. Eckstein, C. Garcia-Rosales, J. Roth, and W. Ottenberger, "Sputtering data," 1993.

[17] D. Nishijima, M. Baldwin, R. Doerner, and J. Yu, "Sputtering properties of tungsten 'fuzzy' surfaces," *Journal of Nuclear Materials*, vol. 415, no. 1, pp. S96–S99, 2011.

[18] S. J. Zenobia, L. M. Garrison, and G. L. Kulcinski, "The response of polycrystalline tungsten to 30 keV helium ion implantation at normal incidence and high temperatures," *Journal of Nuclear Materials*, vol. 425, no. 1-3, pp. 83–92, 2012.

[19] F. Sefta, N. Juslin, K. Hammond, and B. Wirth, "Molecular dynamics simulations on the effect of sub-surface helium bubbles on the sputtering yield of tungsten," *Journal of Nuclear Materials*, vol. 438, pp. S493–S496, 2013.

[20] F. Ferroni, K. D. Hammond, and B. D. Wirth, "Sputtering yields of pure and helium-implanted tungsten under fusion-relevant conditions calculated using molecular dynamics," *Journal of Nuclear Materials*, vol. 458, pp. 419–424, 2015.

[21] Z. Yang, W. Song, Y. Li, and J. Yang, "BCA simulations of ion irradiation of tungsten fuzz," *Nuclear Instruments and Methods in Physics Research Section B: Beam Interactions with Materials and Atoms*, vol. 455, pp. 118–123, 2019.

[22] R. Stadlmayr, P. Szabo, D. Mayer, C. Cupak, T. Dittmar, L. Bischoff, S. Möller, M. Rasiński, R. Wilhelm, W. Möller *et al.*, "Sputtering of nanostructured tungsten and comparison to modelling with TRI3DYN," *Journal of Nuclear Materials*, vol. 532, p. 152019, 2020.

[23] K. Schlueter, K. Nordlund, G. Hobler, M. Balden, F. Granberg, O. Flinck, T. da Silva, and R. Neu, "Absence of a Crystal Direction Regime in which Sputtering Corresponds to Amorphous Material," *Physical Review Letters*, vol. 125, no. 22, p. 225502, 2020.

[24] E. Marenkov, K. Nordlund, I. Sorokin, A. Eksaeva, K. Gutorov, J. Jussila, F. Granberg, and D. Borodin, "Angular and velocity distributions of tungsten sputtered by low energy argon ions," *Journal of Nuclear Materials*, vol. 496, pp. 18–23, 2017.

[25] J. Jussila, F. Granberg, and K. Nordlund, "Effect of random surface orientation on W sputtering yields," *Nuclear Materials and Energy*, vol. 17, pp. 113–122, 2018.

[26] M. Backman, M. Toulemonde, O. H. Pakarinen, N. Juslin, F. Djurabekova, K. Nordlund, A. Debelle, and W. J. Weber, "Molecular dynamics simulations of swift heavy ion induced defect recovery in SiC," *Computational materials science*, vol. 67, pp. 261–265, 2013.

[27] R. Behrisch and W. Eckstein, *Sputtering by particle bombardment: experiments and computer calculations from threshold to MeV energies.* Springer Science & Business Media, 2007, vol. 110.

[28] K. Hattar, "Deformation structures including twins in nanograined pure metals," in *Nanostructured Metals and Alloys.* Elsevier, 2011, pp. 213–242.

[29] E. Martínez and B. P. Uberuaga, "Mobility and coalescence of stacking fault tetrahedra in Cu," *Scientific Reports*, vol. 5, no. 1, pp. 1–5, 2015.

[30] P. Sigmund, "Sputtering by ion bombardment theoretical concepts," in *Sputtering by particle bombardment I.* Springer, 1981, pp. 9–71.

[31] D. Takeuchi, T. Seki, T. Aoki, J. Matsuo, and I. Yamada, "Cluster ion bombardment on atomically flat Au (111) solid surfaces," *Materials chemistry and physics*, vol. 54, no. 1-3, pp. 76–79, 1998.

[32] G. Betz and K. Wien, "Energy and angular distributions of sputtered particles," *International Journal of Mass Spectrometry and Ion Processes*, vol. 140, no. 1, pp. 1–110, 1994.

[33] F. Agulló-López, A. Mendez, G. García, J. Olivares, and J. Cabrera, "Synergy between thermal spike and exciton decay mechanisms for ion damage and amorphization by electronic excitation," *Physical Review B*, vol. 74, no. 17, p. 174109, 2006.

[34] H. Oechsner, "Sputtering – a review of some recent experimental and theoretical aspects," *Applied physics*, vol. 8, no. 3, pp. 185–198, 1975.

[35] P. Sigmund, "Theory of sputtering. I. Sputtering yield of amorphous and polycrystalline targets," *Physical review*, vol. 184, no. 2, p. 383, 1969.

[36] H. Nakamura, S. Saito, and A. M. Ito, "Sputtering yield of noble gas irradiation onto tungsten surface," *Journal of Advanced Simulation in Science and Engineering*, vol. 3, no. 2, pp. 165–172, 2016.

[37] H. Bay and J. Bohdansky, "Sputtering yields for light ions as a function of angle of incidence," *Applied physics*, vol. 19, no. 4, pp. 421–426, 1979.

[38] K. Nordlund, F. Djurabekova, and G. Hobler, "Large fraction of crystal directions leads to ion channeling," *Physical Review B*, vol. 94, no. 21, p. 214109, 2016.

[39] Y. Stark, R. Frömter, D. Stickler, and H. P. Oepen, "Sputter yields of single- and polycrystalline metals for application in focused ion beam technology," *Journal of Applied Physics*, vol. 105, no. 1, p. 013542, 2009.

[40] B. Kempshall, S. Schwarz, B. Prenitzer, L. Giannuzzi, R. Irwin, and F. Stevie, "Ion channeling effects on the focused ion beam milling of Cu," *Journal of Vacuum Science & Technology B: Microelectronics and Nanometer Structures Processing, Measurement, and Phenomena*, vol. 19, no. 3, pp. 749–754, 2001.

[41] M. R. Murty, "Sputtering: the material erosion tool," *Surface Science*, vol. 500, no. 1-3, pp. 523–544, 2002.

[42] G. Bräuer, J. Szczyrbowski, and G. Teschner, "Mid frequency sputtering – a novel tool for large area coating," *Surface and Coatings Technology*, vol. 94, pp. 658–662, 1997.

[43] J. T. Gudmundsson, "The high power impulse magnetron sputtering discharge as an ionized physical vapor deposition tool," *Vacuum*, vol. 84, no. 12, pp. 1360–1364, 2010.

[44] M. Y. Ali, W. Hung, and F. Yongqi, "A review of focused ion beam sputtering," *International journal of precision engineering and manufacturing*, vol. 11, no. 1, pp. 157–170, 2010.

[45] G. K. Wehner, "Sputtering of metal single crystals by ion bombardment," *Journal of Applied Physics*, vol. 26, no. 8, pp. 1056–1057, 1955.

[46] G. K. Wehner, "Controlled sputtering of metals by low-energy Hg ions," *Physical Review*, vol. 102, no. 3, p. 690, 1956.

[47] P. Sigmund, "Recollections of fifty years with sputtering," *Thin Solid Films*, vol. 520, no. 19, pp. 6031–6049, 2012.

[48] R. Silsbee, "Focusing in collision problems in solids," *Journal of Applied Physics*, vol. 28, no. 11, pp. 1246–1250, 1957.

[49] G. Anderson and G. Wehner, "Atom ejection patterns in single-crystal sputtering," *Journal of Applied Physics*, vol. 31, no. 12, pp. 2305–2313, 1960.

[50] W. Eckstein and J. Laszlo, "Sputtering of tungsten and molybdenum," *Journal of nuclear materials*, vol. 183, no. 1-2, pp. 19–24, 1991.

[51] C. Wu and E. Hechtl, "Erosion of tungsten by self-sputtering and light ion irradiation at oblique angles of incidence," *Journal of nuclear materials*, vol. 196, pp. 569–572, 1992.

[52] E. Salonen, K. Nordlund, J. Keinonen, and C. Wu, "Molecular dynamics studies of the sputtering of divertor materials," *Journal of nuclear materials*, vol. 313, pp. 404–407, 2003.

[53] J. Drobny and D. Curreli, "F-TRIDYN simulations of tungsten self-sputtering and applications to coupling plasma and material codes," *Computational Materials Science*, vol. 149, pp. 301–306, 2018.

[54] E. Salonen, K. Nordlund, J. Keinonen, and C. Wu, "Enhanced erosion of tungsten by atom clusters," *Journal of nuclear materials*, vol. 305, no. 1, pp. 60–65, 2002.

[55] C. Wu and U. Mszanowski, "A comparison of lifetimes of beryllium, carbon, molybdenum and tungsten as divertor armour materials," *Journal of nuclear materials*, vol. 218, no. 3, pp. 293–301, 1995.

[56] M. Saidoh and K. Sone, "Low energy selfsputtering yields of molybdenum and tungsten," *Japanese journal of applied physics*, vol. 22, no. 9R, p. 1361, 1983.

[57] J. Biersack and W. Eckstein, "Sputtering studies with the Monte Carlo program TRIM.SP," *Applied Physics A*, vol. 34, no. 2, pp. 73–94, 1984.

[58] H. Bay, J. Bohdansky, W. Hofer, and J. Roth, "Angular distribution and differential sputtering yields for low-energy light-ion irradiation of polycrystalline nickel and tungsten," *Applied physics*, vol. 21, no. 4, pp. 327–333, 1980.

[59] X. Yang and A. Hassanein, "Atomic scale calculations of tungsten surface binding energy and beryllium-induced tungsten sputtering," *Applied surface science*, vol. 293, pp. 187–190, 2014.

[60] M. Baldwin and R. Doerner, "Helium induced nanoscopic morphology on tungsten under fusion relevant plasma conditions," *Nuclear Fusion*, vol. 48, no. 3, p. 035001, 2008.

[61] J. Ziegler, J. J. Cuomo, and J. Roth, "Reduction of ion sputtering yield by special surface microtopography," *Applied Physics Letters*, vol. 30, no. 6, pp. 268–271, 1977.

[62] J. F. Ziegler, J. P. Biersack, and M. D. Ziegler, the Stopping and Range of Ions in Matter, SRIM, http://www.srim.org.

[63] K. Sugiyama, K. Schmid, and W. Jacob, "Sputtering of iron, chromium and tungsten by energetic deuterium ion bombardment," *Nuclear Materials and Energy*, vol. 8, pp. 1–7, 2016.

[64] A. P. Thompson, H. M. Aktulga, R. Berger, D. S. Bolintineanu, W. M. Brown, P. S. Crozier, P. J. in 't Veld, A. Kohlmeyer, S. G. Moore, T. D. Nguyen, R. Shan, M. J. Stevens, J. Tranchida, C. Trott, and S. J. Plimpton, "LAMMPS - a flexible simulation tool for particle-based materials modeling at the atomic, meso, and continuum scales," *Comp. Phys. Comm.*, vol. 271, p. 108171, 2022.

[65] T. Sizyuk and A. Hassanein, "Dynamic analysis and evolution of mixed materials bombarded with multiple ions beams," *Journal of nuclear materials*, vol. 404, no. 1, pp. 60–67, 2010.

[66] K. Nordlund, 2010, PARCAS computer code. The main principles of the molecular dynamics algorithms are presented in [93, 94]. The adaptive time step and electronic stopping algorithms are the same as in [95].

[67] Supplemental material to [23], found at http://link.aps.org/supplemental/10.1103/PhysRevLett.125.225502.

[68] G. Hobler, "Monte Carlo simulation of two-dimensional implanted dopant distributions at mask edges," *Nuclear Instruments and Methods in Physics Research Section B: Beam Interactions with Materials and Atoms*, vol. 96, no. 1-2, pp. 155–162, 1995.

[69] D. Meluzova, P. Y. Babenko, A. Zinoviev, and A. Shergin, "Sputtering of Tungsten by Beryllium and Neon Ions," *Technical Physics Letters*, vol. 46, no. 12, pp. 1227–1230, 2020.

[70] S. Saito, H. Nakamura, and M. Tokitani, "Comparison of induced damage, range, reflection, and sputtering yield between amorphous, BCC crystalline, and bubble-containing tungsten materials under hydrogen isotope and noble gas plasma irradiations," *Japanese Journal of Applied Physics*, vol. 56, no. 1S, p. 01AF04, 2016.

[71] J. E. Lennard-Jones, "On the forces between atoms and ions," *Proceedings of the Royal Society of London. Series A, Containing Papers of a Mathematical and Physical Character*, vol. 109, no. 752, pp. 584–597, 1925.

[72] J. E. Lennard-Jones and B. M. Dent, "The forces between atoms and ions.–II," *Proceedings of the Royal Society of London. Series A, Containing Papers of a Mathematical and Physical Character*, vol. 112, no. 760, pp. 230–234, 1926.

[73] P. M. Morse, "Diatomic molecules according to the wave mechanics. II. Vibrational levels," *Physical review*, vol. 34, no. 1, p. 57, 1929.

[74] F. H. Stillinger and T. A. Weber, "Computer simulation of local order in condensed phases of silicon," *Physical review B*, vol. 31, no. 8, p. 5262, 1985.

[75] J. Tersoff, "New empirical model for the structural properties of silicon," *Physical review letters*, vol. 56, no. 6, p. 632, 1986.

[76] J. Tersoff, "New empirical approach for the structure and energy of covalent systems," *Physical review B*, vol. 37, no. 12, p. 6991, 1988.

[77] M. S. Daw and M. I. Baskes, "Embedded-atom method: Derivation and application to impurities, surfaces, and other defects in metals," *Physical Review B*, vol. 29, no. 12, p. 6443, 1984.

[78] D. W. Brenner, "Empirical potential for hydrocarbons for use in simulating the chemical vapor deposition of diamond films," *Physical review B*, vol. 42, no. 15, p. 9458, 1990.

[79] M. Finnis and J. Sinclair, "A simple empirical N-body potential for transition metals," *Philosophical Magazine A*, vol. 50, no. 1, pp. 45–55, 1984.

[80] M. I. Baskes, "Modified embedded-atom potentials for cubic materials and impurities," *Physical review B*, vol. 46, no. 5, p. 2727, 1992.

[81] L. Verlet, "Computer "experiments" on classical fluids. I. Thermodynamical properties of Lennard-Jones molecules," *Physical review*, vol. 159, no. 1, p. 98, 1967.

[82] R. Hockney and J. Eastwood, "Computer Simulation Using Particles," *Computer Simulation Using Particles*, 1981.

[83] W. C. Swope, H. C. Andersen, P. H. Berens, and K. R. Wilson, "A computer simulation method for the calculation of equilibrium constants for the formation of physical clusters of molecules: Application to small water clusters," *The Journal of chemical physics*, vol. 76, no. 1, pp. 637–649, 1982.

[84] C. W. Gear, "Numerical initial value problems in ordinary differential equations," *Prentice-Hall series in automatic computation*, 1971.

[85] R. Komanduri and L. Raff, "A review on the molecular dynamics simulation of machining at the atomic scale," *Proceedings of the Institution of Mechanical Engineers, Part B: Journal of Engineering Manufacture*, vol. 215, no. 12, pp. 1639–1672, 2001.

[86] H. J. Berendsen, J. v. Postma, W. F. van Gunsteren, A. DiNola, and J. R. Haak, "Molecular dynamics with coupling to an external bath," *The Journal of chemical physics*, vol. 81, no. 8, pp. 3684–3690, 1984.

[87] S. C. Harvey, R. K.-Z. Tan, and T. E. Cheatham III, "The flying ice cube: velocity rescaling in molecular dynamics leads to violation of energy equipartition," *Journal of computational chemistry*, vol. 19, no. 7, pp. 726–740, 1998.

[88] S. Nosé, "A unified formulation of the constant temperature molecular dynamics methods," *The Journal of chemical physics*, vol. 81, no. 1, pp. 511–519, 1984.

[89] W. G. Hoover, "Canonical dynamics: Equilibrium phase-space distributions," *Physical review A*, vol. 31, no. 3, p. 1695, 1985.

[90] M.-C. Marinica, L. Ventelon, M. Gilbert, L. Proville, S. Dudarev, J. Marian, G. Bencteux, and F. Willaime, "Interatomic potentials for modelling radiation defects and dislocations in tungsten," *Journal of Physics: Condensed Matter*, vol. 25, no. 39, p. 395502, 2013.

[91] A. E. Sand, J. Dequeker, C. Becquart, C. Domain, and K. Nordlund, "Non-equilibrium properties of interatomic potentials in cascade simulations in tungsten," *Journal of Nuclear Materials*, vol. 470, pp. 119–127, 2016.

[92] A. Stukowski, "Visualization and analysis of atomistic simulation data with OVITO–the Open Visualization Tool," *Modelling and simulation in materials science and engineering*, vol. 18, no. 1, Jan 2010.

[93] K. Nordlund, M. Ghaly, R. S. Averback, M. Caturla, T. Diaz de la Rubia, and J. Tarus, "Defect production in collision cascades in elemental semiconductors and FCC metals," *Phys. Rev. B*, vol. 57, no. 13, pp. 7556–7570, 1998.

[94] M. Ghaly, K. Nordlund, and R. S. Averback, "Molecular dynamics investigations of surface damage produced by keV self-bombardment of solids," *Phil. Mag. A*, vol. 79, no. 4, p. 795, 1999.

[95] K. Nordlund, "Molecular dynamics simulation of ion ranges in the $1 - 100$ keV energy range," *Comput. Mater. Sci.*, vol. 3, p. 448, 1995.